

Distinguishing models of reionization using future radio observations of 21-cm 1-point statistics

C. A. Watkinson^{1*} & J. R. Pritchard¹

¹*Department of Physics, Blackett Laboratory, Imperial College, London SW7 2AZ, UK*

24 August 2021

ABSTRACT

We explore the impact of reionization topology on 21-cm statistics. Four reionization models are presented which emulate large ionized bubbles around over-dense regions (21CMFAST/global-inside-out), small ionized bubbles in over-dense regions (local-inside-out), large ionized bubbles around under-dense regions (global-outside-in) and small ionized bubbles around under-dense regions (local-outside-in). We show that first generation instruments might struggle to distinguish global models using the shape of the power spectrum alone. All instruments considered are capable of breaking this degeneracy with the variance, which is higher in outside-in models. Global models can also be distinguished at small scales from a boost in the power spectrum from a positive correlation between the density and neutral-fraction fields in outside-in models. Negative skewness is found to be unique to inside-out models and we find that pre-SKA instruments could detect this feature in maps smoothed to reduce noise errors. The early, mid and late phases of reionization imprint signatures in the brightness-temperature moments, we examine their model dependence and find pre-SKA instruments capable of exploiting these timing constraints in smoothed maps. The dimensional skewness is introduced and is shown to have stronger signatures of the early and mid-phase timing if the inside-out scenario is correct.

Key words: Key words: dark ages, reionization, first stars – intergalactic medium – methods: statistical – cosmology: theory.

1 INTRODUCTION

We live in a time when we have a seemingly excellent understanding of the Universe in which we reside. The Planck experiment (Planck Collaboration 2013) find the Lambda Cold Dark Matter (Λ CDM) paradigm to be an excellent fit to observations of the cosmic microwave background (CMB), constraining the six parameters that describe this model to percent level accuracy. The CMB decoupled from matter approximately 380,000 years after the Big Bang and so is sensitive to the conditions of the early Universe; subsequent interactions with the rest of the Universe’s energy content imprinted signatures that provide insight into the evolution of the Universe. However, there exists a gap in our understanding of this evolution that needs filling: the epoch of reionization (EoR), during which the intergalactic medium (IGM) transitioned from being completely neutral after the CMB decoupled to become completely ionized around a billion years after the Big Bang. We refer the reader to Barkana & Loeb (2001) and Loeb & Furlanetto (2013) for a good introduction to reionization.

The reionization process is complex, sensitive to many uncertainties such as the nature and evolution of the sources responsible,

(e.g. Robertson et al. 2013), the degree to which the IGM clumped into dense neutral sinks of ionising radiation (e.g. Miralda-Escude et al. 2000; Furlanetto & Oh 2005), and modulation (if any) from feedback effects (e.g. Efstathiou 1992; Haiman et al. 2000; Dijkstra et al. 2004); even the detailed timing of the overall process remains an open question. Given this uncertainty, it is vital that we fully explore all possible aspects of this process so that our interpretation of reionization related observations are well informed.

We have some observational constraints on the epoch of reionization. Thomson scattering of CMB photons by free electrons produced during reionization wash out temperature fluctuations and induce large scale polarization anisotropies. This provides constraints on the integral optical depth to the CMB last scattering surface, indicating that reionization must have been under way by $z \sim 11$ (Planck Collaboration 2013; Bennett et al. 2013); this assumes instantaneous reionization, which is unlikely to be a realistic scenario. Measurements from the thermal history of the IGM are consistent with this figure (Theuns et al. 2002; Bolton et al. 2010; Lidz et al. 2010).

Measurements of the Lyman- α forest in high redshift quasars indicate that reionization was finished by $z \sim 6.5$ (Becker et al. 2001; Fan et al. 2002, 2006) and the detection of a Lyman- α damping wing and small proximity zone in the most distant known

* Email: c.watkinson11@imperial.ac.uk

quasar at $z = 7.085$ is consistent with an IGM neutral fraction of more than 10% (Bolton et al. 2011; Mortlock et al. 2011). The existing constraints from quasars have been bolstered by hints from an apparent deficit of Lyman- α emitters that the neutral fraction is above 10% by $z \sim 7$ (Ota et al. 2010; Pentericci et al. 2011; Ono et al. 2012; Schenker et al. 2012).

To improve constraints on the epoch of reionization, work is under way to exploit the weak imprint of the H I 21-cm spectral line on the CMB. This transition results from a spin flip in neutral hydrogen's lowest energy level, corresponding to a rest-frame wavelength $\lambda \approx 21.1$ cm and frequency $\nu \approx 1420.4$ MHz (Ewen & Purcell 1951; Prodel & Kusch 1952). As is usual in radio observations, radiation intensity I_ν is described in terms of brightness temperature, T_b , defined such that $I_\nu = B(T_b)$; $B(T)$ is the Planck black-body spectrum and is well approximated by the Rayleigh-Jeans formula at the frequencies relevant to reionization studies.

The measured quantity is the differential brightness temperature $\delta T_b = T_b - T_\gamma$ along a line of sight, where T_γ is the temperature of the CMB. This differential brightness temperature evolves according to (Field 1958, 1959; Madau et al. 1997),

$$\begin{aligned} \delta T_b &= \frac{T_s - T_\gamma}{1+z} (1 - e^{-\tau_{\nu_0}}) \\ &\approx 27. \frac{T_s - T_\gamma}{T_s} x_{\text{HI}} (1 + \delta) \left[\frac{H(z)/(1+z)}{dv_r/dr} \right] \\ &\quad \times \left(\frac{1+z}{10} \frac{0.15}{\Omega_m h^2} \right)^{1/2} \left(\frac{\Omega_b h^2}{0.023} \right) \text{mK}. \end{aligned} \quad (1)$$

This quantity is dependent on the neutral fraction of hydrogen x_{HI} , the matter overdensity δ , line of sight velocity gradient dv_r/dr , Hubble parameter $H(z)$, matter density parameter Ω_m , and baryon density parameter Ω_b ; $\Omega_i = \rho_i/\rho_c$ where ρ_c is the critical density required for flat universe. The differential temperature also depends on the gas spin temperature T_s , which measures the occupation levels of the two hyperfine energy levels involved in the H I 21-cm line and determines the 21-cm optical depth τ_{ν_0} . We will neglect this dependence by assuming $T_s \gg T_\gamma$, i.e. the neutral gas has been heated well above the CMB for the redshift range considered (Pritchard & Loeb 2008). However, it is quite possible that spin-temperature fluctuations may be influential during reionization (Pritchard & Furlanetto 2007), we defer this question to future work. For a comprehensive review of the 21-cm line we refer the reader to Furlanetto et al. (2006); Morales & Wyithe (2010) and Pritchard & Loeb (2011).

There are many radio telescopes operating, under construction, or in the design stages that aim to measure the 21-cm line, e.g. the Murchison Wide-field Array¹ (MWA), the LOw Frequency ARray² (LOFAR), the Precision Array to Probe Epoch of Reionization³ (PAPER), the Giant Meter-wave Radio Telescope⁴ (GMRT), and the Square Kilometre Array⁵ (SKA). All aim to detect radio fluctuations in the redshifted 21-cm signal that correspond to varying levels of neutral hydrogen. The signal from reionization will only be probed at a statistical level by pre-SKA telescopes. Next generation instruments, such as SKA, will make detailed maps of the 21-cm signal, enabling the measurement of hydrogen's properties

out to $z = 25$. Such observations will constrain the properties of the intergalactic medium (IGM) and therefore the cumulative effect of all sources of light.

There has been much focus on the statistics of the 21-cm signal produced by the process of reionization, along with their detectability by future observations; previous studies have looked at the power spectrum (e.g. Furlanetto et al. 2004; Zaldarriaga et al. 2004; Mellema et al. 2006; Lidz et al. 2008; Pritchard & Loeb 2008; Mesinger et al. 2011; Friedrich et al. 2011), the probability density function (PDF) and its moments (e.g. Furlanetto et al. 2004; Wyithe & Morales 2007; Harker et al. 2009; Ichikawa et al. 2010), and the difference PDF (e.g. Barkana & Loeb 2008; Pan & Barkana 2012). This is mainly because we will be limited to statistical measures in the near future, but even with the precision of SKA, statistics will play a vital role in connecting theory to observation.

Despite the consensus of different observations that we are observing the end of reionization at $z > 6$, the effect of absorption systems casts uncertainty on this by adjusting the mean free path at high redshifts. The nature of such absorbers could also strongly affect the morphology and environment of the ionized regions throughout reionization (Crociani et al. 2010; Alvarez & Abel 2012).

In this work we test the sensitivity of various statistics to different morphological characteristics of ionized regions that might have formed during reionization. We take 21CMFAST (Mesinger et al. 2011) as our reference model, the properties of which are large ionized regions around the over-dense regions containing sources. We then construct three contrasting toy models: one with small ionized bubbles in over-dense regions; one with small ionized bubbles in under-dense regions; and another with large ionized bubbles in under-dense regions. The truth will likely be a combination of such properties, with large-scale inside-out behaviour contrasted by recombination effects producing outside-in behaviour on smaller scales, e.g. Furlanetto & Oh (2005). By examining the statistics of the extreme models described in this work, we are able to tease apart the effects of each property, and therefore understand the strengths and limitations of each statistic.

We examine the power spectrum, 1-dimensional PDF, skewness and variance of 21-cm maps, as well as the maps themselves; we place emphasis on the model dependent differences in these statistics. To approximate instrumental effects we smooth and re-sample the maps according to the likely instrumental resolution of MWA, LOFAR and SKA. Errors induced by instrumental noise are then approximated by assuming independent but identically distributed random Gaussian noise with zero mean on each pixel and propagating these brightness-temperature errors on to our statistics. Finally, the variability in the statistics caused by cosmic variance is estimated by sub-sampling.

This rest of this paper is structured as follows: in Section 2 we detail the four models we use to simulate the different reionization scenarios; in Section 3 we construct an illustrative toy model for the PDF of the neutral-fraction maps and compare the moments of this toy model with those measured from our four model simulations; we then move on to maps of brightness temperature, first looking at the statistics of clean maps in Section 4; then, in Section 5, we study the statistics of noisy maps that mimic instrumental effects; we look at the limitations imposed by cosmic variance in section 6; and finally, in Section 7 we discuss our conclusions. Unless stated otherwise all lengths are co-moving. Throughout we assume a standard Λ CDM cosmology as constrained by Planck,

¹ <http://www.mwatelescope.org/>

² <http://www.lofar.org/>

³ <http://eor.berkeley.edu/>

⁴ <http://gmrt.ncra.tifr.res.in/>

⁵ <http://www.skatelescope.org/>

adopting $\sigma_8 = 0.829$, $h = 0.673$, $\Omega_m = 0.315$, $\Omega_\Lambda = 0.685$, $\Omega_b = 0.049$ and $n_s = 0.96$ (Planck Collaboration 2013).

2 MODELS FOR REIONIZATION

We utilise four simulations to mimic the behaviour of different plausible ways in which ionized bubbles might have evolved with time. Our aim here is not to produce a detailed and accurate simulation of reionization, instead the qualitatively different models that we describe in this section allow clean separation of the effect that different morphological properties have on the statistics of the 21-cm brightness temperature. In reality, the characteristics we discuss in this chapter will not be as extreme and will likely be present in combination with others. Table 1 presents a summary of the physical motivation behind each model, defined by the interplay between ionization and recombination.

The idea of global reionization in which over-dense regions are ionized first is preferred by current theory and simulations; as such we use the well established semi-numerical code 21CMFAST (Mesinger & Furlanetto 2007; Mesinger et al. 2011) to provide a density field and our fiducial global-inside-out model. We then use this density field as a skeleton upon which to construct global-outside-in, local-inside-out and local-outside-in models. We neglect spin-temperature fluctuations so that the contributors to fluctuations in the 21-cm brightness temperature are the neutral-fraction field x_{HI} , the velocity field dv_r/dr and the density field δ . The four models we use differ only in the prescription used to construct the neutral-fraction field and thus have identical density and velocity fields. The inside-out models have density fields that are anti-correlated with the neutral-fraction field, with the most dense regions being the least likely to remain neutral. In contrast, outside-in models have density fields correlated with the neutral field so that regions of extreme overdensity will instead host the most persistent neutral regions. Where there is sensitivity to the global properties of the density field, larger bubbles of ionized gas will develop; in contrast if there is only localised sensitivity then these bubbles will be much smaller.

2.1 Global-inside-out: 21CMFAST

21CMFAST numerically implements the approach of Furlanetto et al. (2004), henceforth FZH04, this paper applied the excursion set formalism to the problem of reionization.

The excursion set model considers the evolution of the matter overdensity field $\delta(\mathbf{r}, R_{\text{smooth}})$, a function of position vector \mathbf{r} and smoothing scale R_{smooth} , with its variance $\sigma^2(R_{\text{smooth}})$. FZH04 constructed a barrier for ionization in overdensity as a function of smoothing scale, illustrated by the red line in Figure 1; the hatched area above depicts the parameter space for which a region would be ionized. The first up-crossing of this barrier (when smoothing from large to small scales) is related to an ionized region of corresponding mass and scale. To construct this barrier they make the simple ansatz that a region will be fully ionized if enough photons have been produced to ionize every baryon in that region, i.e. it is able to self ionize. The mass of an ionized region m_{ion} is then related to the mass in collapsed objects m_{gal} by an efficiency factor ζ according to,

$$m_{\text{ion}} = \zeta m_{\text{gal}}. \quad (2)$$

The efficiency factor parametrizes the efficiency at which ionizing

Table 1. Summary of the four models considered in this paper.

Figure key	Model motivation
global-inside-out Figure 1 : Region is ionized at first up-crossing of red barrier.	<i>21CMFAST</i> UV-fuelled ionized bubbles form and grow around the over-dense regions containing ionizing sources. The growth of these ionized bubbles drives the decrease in the average neutral fraction during the course of reionization
local-inside-out Figure 1 : Pixel is ionized if its over-density is above blue threshold.	<i>pixel-by-pixel inversion of MHR00</i> A high density of absorbers keep the mean free path of the UV photons small; ionized regions are limited to the immediate neighbourhood of the originator galaxy of ionizing radiation. The average neutral fraction decreases with time as the ionizing photons from more and more UV sources are able to overpower the recombinations/absorbers in their individual haloes.
global-outside-in Figure 1 : Region is ionized at first down-crossing of dotted black barrier.	<i>Inversion of 21CMFAST</i> High recombination rates in over-dense regions mean that stable ionized bubbles form in the under-dense regions. An increasingly intense background of hard radiation overwhelms recombination rates on the higher density outskirts of these bubbles and they grow, decreasing the average neutral fraction with time.
local-outside-in Figure 1 : Pixel is ionized if its over-density is below green threshold.	<i>pixel-by-pixel implementation of MHR00</i> Recombinations and/or absorbers dominate and only under-dense regions in very localised regions become ionized. The average neutral fraction decreases with time as increasingly intense background of hard radiation overpowers the recombinations/absorbers in more and more regions.

photons will escape a collapsed object, which depends on uncertain source properties and could be a function of time. An insightful interpretation is to write $\zeta = f_{\text{esc}} f_* N_{\gamma/b} (1 + n_{\text{rec}})^{-1}$, where f_{esc} is the fraction of ionizing photons that escape the object, f_* is the star formation efficiency of the object, $N_{\gamma/b}$ denotes the number of ionizing photons produced per baryon in stars, and finally n_{rec} is the typical number of times that hydrogen will have recombined. FZH04 used the assumption of equation 2 to set up a condition for ionization by requiring that a fully ionized region have a collapsed fraction $f_{\text{coll}} \geq \zeta^{-1}$; the collapsed fraction can be thought of as the fraction of a region that contains ionizing sources. Rearranging the extended Press–Schechter prediction for f_{coll} (Bond et al. 1991; Lacey & Cole 1993) gives the ionization barrier

$$\delta_m \geq \delta_x(m, z) \equiv \delta_c(z) - \sqrt{2}K(\zeta) [\sigma_{\text{min}}^2 - \sigma_m^2]^{1/2}, \quad (3)$$

in which $K(\zeta) = \text{erf}^{-1}(1 - \zeta^{-1})$, $\delta_c(z)$ is the critical density for gravitational collapse, σ_m^2 is the variance of density fluctuation on the scale $m(R_{\text{smooth}})$, δ_m is the mean overdensity in the region, and $\sigma_{\text{min}}^2 = \sigma^2(m_{\text{min}})$, where m_{min} is the minimum mass for collapse.

The key implication of this model is that for every redshift there is a preferred scale for ionized regions. This occurs because there is a ‘sweet spot’ for first crossings; a positive gradient makes

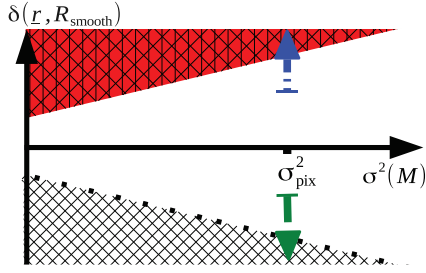


Figure 1. Illustration of the barriers for ionization in overdensity against variance on a given smoothing scale $\sigma^2(R_{\text{smooth}})$. Barriers relate to global-inside-out (solid red line with hatching above), local-inside-out (blue dotted arrow), global-outside-in (black dashed line with hatching below) and local-outside-in (green dashed arrow).

the barrier easier to cross at large scales, where sufficiently large overdensities are rare, than it is to cross at the smaller scales where overdensities are more extreme. As the barrier moves down with decreasing redshift, ionized regions become more numerous and the characteristic size shifts to larger scales.

This approach was utilised in the semi-numerical 21CMFAST simulation package (Mesinger & Furlanetto 2007; Mesinger et al. 2011). This generates density and velocity fields from Gaussian initial conditions and then approximates gravitational collapse using first order perturbation theory (Zel’dovich 1970) to produce non-linear density maps. 21CMFAST then numerically applies the excursion-set approach of FZH04 to construct its neutral-fraction fields from the density fields. The code smooths the density field concentrically from a maximum allowed radius for a cohesive ionized region $R_{\text{max}} \approx 30\text{Mpc}$ ⁶, down to that of a pixel R_{pix} . At each smoothing scale it checks which pixels meet the condition $f_{\text{coll}}(\mathbf{r}, z, R_{\text{smooth}}) \geq \zeta^{-1}$ where \mathbf{r} denotes position and flags them to be ionized if they do. After the final filtering step, pixels which have not yet been marked as fully ionized are allocated a value of $x_{\text{HI}} = 1 - \zeta f_{\text{coll}}(\mathbf{r}, z, R_{\text{pix}})$, with the physical constraint that $0 \leq x_{\text{HI}} \leq 1$ to allow for partial ionization.

Once the neutral-fraction, density and differential velocity maps are calculated it is straightforward to calculate the brightness-temperature map by applying equation 1 to every pixel. For a detailed description of this code we refer the reader to the 21CMFAST references quoted at the beginning of this section.

2.2 Local-outside-in: Pixel by pixel MHR00

To construct outside-in models, in which under-dense regions are ionized first, we follow the general ideas outlined by Miralda-Escude et al. (2000) hereafter MHR00. The crucial concept in their model was that of a global recombination rate that is an increasing function of δ . They imagine that all gas with a $\delta < \delta_{\text{ion}}$ is ionized, whilst higher density gas is neutral due to this global recombination rate; δ_{ion} is thus a threshold for ionization. Sources located in high-density regions, i.e. galaxies, first ionize the dense gas of the galactic halo after which the ionizing photons begin to infiltrate into the IGM. Since there are both less atoms to ionize and fewer recombinations in low density regions, H II regions expand most

quickly along directions of lowest gas density. The end of reionization is reached when ionized regions start overlapping and most of the IGM is illuminated by more than one source; such overlap will occur in the lowest density ‘tunnels’ that exist between sources.

To make a local version of the MHR00 model, we first smooth the density boxes generated from 21CMFAST with a k-space top-hat filter on a radius of 0.75Mpc; this scale corresponds roughly to the Jeans length of $\sim 1\text{Mpc}$ for a gas temperature of $\sim 10^4\text{K}$ (Jeans 1928). The density box is numerical in nature, randomly generated from power spectrum initial conditions and suffers from discretisation issues arising during the perturbation of mass that accounts for non-linear evolution; smoothing counteracts these effects and makes the density maps more physical.

We next establish the density threshold necessary to reproduce the volume-averaged neutral fraction \bar{x}_{HI} from our 21CMFAST simulation when ionizing individual pixels whose overdensities satisfy $\delta < \delta_{\text{ion}}$. The threshold for ionization, δ_{ion} , is defined to be the overdensity in the i^{th} pixel that satisfies $i/N_{\text{pix}} = 1 - \bar{x}_{\text{HI}}$ when the pixels are sorted into ascending order and N_{pix} is the total number of pixels. Finally, we create the x_{HI} map by ionizing all pixels that meet the condition $\delta < \delta_{\text{ion}}$. Once we have our neutral-fraction maps we can generate the corresponding brightness-temperature maps.

2.3 Local-inside-out: pixel-by-pixel MHR00 inversion

In creating a localised inside-out model we simply invert the ionization condition of the local-outside-in model to $\delta > \delta'_{\text{ion}}$. Again, we fix the threshold to ensure that the box has the desired neutral fraction. This is implemented with same method as the local-outside-in model, except with the density pixels in descending order. Once we have δ'_{ion} , we can simply cycle through pixels and ionize any that meet the above condition. The corresponding brightness-temperature maps can then be calculated.

2.4 Global-outside-in: Inverting 21CMFAST

The framework of FZH04 can be used to enforce the prescription of MHR00 in a way that is sensitive to the large-scale nature of the density field. We suppose that over-dense regions have too high a recombination rate for ionized regions to form and develop, instead a background of ionizing radiation of efficiency ζ_{bg} ionizes under-dense regions of the IGM; this efficiency factor can be parametrized in a similar way to that of FZH04 but in the context of more energetic radiation. We assume a critical density δ''_{ion} below which the recombination rate in a region is low enough for an ionized bubble to develop. We take the overdensity field to be a function of position and smoothing scale (R_{smooth}) to consider f_{low} , the fraction of matter on a given scale with $\delta(\mathbf{r}, R_{\text{smooth}}) \leq \delta''_{\text{ion}}$. There is no clearly defined value that this critical density should take, so we choose $\delta''_{\text{ion}} = -\delta_c$ to aid in comparison with our other models. Given a region of mean overdensity δ_m the PDF is $\exp[-(\delta - \delta_m)^2 / 2(\sigma_{\text{min}}^2 - \sigma_m^2)] / \sqrt{2\pi(\sigma_{\text{min}}^2 - \sigma_m^2)}$, where we adopt the same notation as in section 2.1. The fraction in a region that is sufficiently under-dense to potentially be ionized is then

$$f_{\text{low}} = \int_{-\infty}^{-\delta_c} d\delta \frac{2}{\sqrt{2\pi(\sigma_{\text{min}}^2 - \sigma_m^2)}} \exp\left[\frac{-(\delta - \delta_m)^2}{2(\sigma_{\text{min}}^2 - \sigma_m^2)}\right]. \quad (4)$$

⁶ R_{max} is a free parameter based on ionized photon mean free path at the redshifts of interest, see Storrie-Lombardi et al. (1994); Miralda-Escude (2003); Choudhury et al. (2008)

The factor of two arises from trajectories that reach the barrier but reflect, in this case, upwards (Bond et al. 1991). By making the substitution $x = (\delta - \delta_m)/\sqrt{2(\sigma_{\min}^2 - \sigma_m^2)}$ we can write $f_{\text{low}} = 2/\sqrt{\pi} \int_{-\infty}^{x_c} \exp(-x^2) dx$, where $x_c = -(\delta_c + \delta_m)/\sqrt{2(\sigma_{\min}^2 - \sigma_m^2)}$, which is refined as follows,

$$\begin{aligned} f_{\text{low}} &= \frac{2}{\sqrt{\pi}} \left[\int_{-\infty}^0 \exp(-x^2) dx + \int_0^{x_c} \exp(-x^2) dx \right] \\ &= 1 + \text{erf}(x_c) = 1 - \text{erf}(-x_c) \\ &= \text{erfc} \left[\frac{(\delta_c + \delta_m)}{\sqrt{2(\sigma_{\min}^2 - \sigma_m^2)}} \right]. \end{aligned} \quad (5)$$

The mass ionized in our underdensity is then related to the efficiency of the ionizing photons by $m_{\text{ion}} = \zeta_{\text{bg}} m_{\text{low}}$ so that

$$f_{\text{low}} = \frac{m_{\text{low}}}{m_{\text{total}}} = \zeta_{\text{bg}}^{-1} \frac{m_{\text{ion}}}{m_{\text{total}}} = \zeta_{\text{bg}}^{-1} f_{\text{ion}}; \quad (6)$$

so for a region to be fully ionized we require $f_{\text{low}} \geq \zeta_{\text{bg}}^{-1}$. This translates into a barrier for ionization as follows,

$$\begin{aligned} \text{erfc} \left[\frac{(\delta_c + \delta_m)}{\sqrt{2(\sigma_{\min}^2 - \sigma_m^2)}} \right] &\geq \zeta_{\text{bg}}^{-1}, \\ \text{erf}^{-1}(1 - \zeta_{\text{bg}}^{-1}) &\geq \frac{(\delta_c + \delta_m)}{\sqrt{2(\sigma_{\min}^2 - \sigma_m^2)}}, \quad (7) \\ \sqrt{2(\sigma_{\min}^2 - \sigma_m^2)} \text{erf}^{-1}(1 - \zeta_{\text{bg}}^{-1}) &\geq \delta_c + \delta_m, \end{aligned}$$

and so our barrier is simply the inverse of the FZH04 barrier with the first down-crossing corresponding to ionized regions,

$$\delta_m \leq \sqrt{2(\sigma_{\min}^2 - \sigma_m^2)} K(\zeta_{\text{bg}}) - \delta_c, \quad (8)$$

where $K(\zeta_{\text{bg}}) = \text{erf}^{-1}(1 - \zeta_{\text{bg}}^{-1})$. This is applied numerically by smoothing the density fields from large to small scales, at each smoothing scale ionizing any pixel that meet the condition of equation 8. At the end, any pixels that remain neutral are assigned a partial neutral fraction according to $x_{\text{HI}} = 1 - \zeta_{\text{bg}} f_{\text{low}}$ under the constraint $0 \leq x_{\text{HI}} \leq 1$. For our simulations we choose that ζ_{bg} take the same value as the efficiency parameter ζ of FZH04. This construction is of course somewhat artificial in that we choose our free variables to match those of FZH04 to aid model comparison and we emphasize that there is no physical basis for these choices. The key prediction of characteristic sizes from the FZH04 model is a product of the increasing barrier. Our barrier, illustrated by the dashed black line of Figure 1, instead decreases with $\sigma^2(M)$; because it is first down-crossings with which we are concerned, the effect is identical and a different choice for the barrier height will not alter this.

Being a mirror of the standard FZH04 approach, one might expect the resulting neutral fraction to be identical. In reality there are differences in that the simulated density field includes non-linearities which have a different impact in an outside-in model, where the neutral field is correlated to the density field, to the anti-correlated inside-out model. Furthermore, 21CMFAST directly tests the condition $f_{\text{coll}} \geq \zeta_{\text{esc}}$ rather than using the barrier; in doing so

it calculates the analytic Press–Schechter f_{coll} . Since the parametrically fitted Sheth & Tormen (1999) mass function of Jenkins et al. (2001) has better agreement to numerical simulations, a correction factor, $A^{\text{PS/J}}$, is applied. This correction can be folded into the ionizing efficiency of our global-outside-in model, but as it is not essential to generating large characteristic sized bubbles we choose to not include it. We thus find that the evolution of the mean neutral fraction with redshift, while close, is not identical to the other models. For this reason and because the volume-averaged ionized fraction $\bar{x}_{\text{ion}} = 1 - \bar{x}_{\text{HI}}$ is an increasing function of time we present all results as functions of average ionized fraction.

2.5 Simulation outline

The box size of all simulations is 300 Mpc on a side, initial conditions are sampled on to a high resolution 1200^3 pixel grid and all subsequent boxes are generated on a 600^3 pixel grid resolving 0.5 Mpc. This simulation size and resolution is competitive and should be large enough to capture the important features of reionization cf. Harker et al. (2009); Bittner & Loeb (2011); Friedrich et al. (2011); Zaroubi et al. (2012); Iliev et al. (2013).

The fiducial 21CMFAST, global-inside-out simulation uses $\zeta = 16$. This choice generates a best-case scenario in which evolution is strongest at the redshifts of optimum sensitivity for MWA and LOFAR, whilst ensuring that reionization is complete by $z \approx 6$; our results are therefore optimistic.

We simulate from a redshift of 6 up to 14.75 in increments of $\Delta z = 0.25$. We analyse the full 3D boxes and so neglect any evolution with redshift that might occur over 300 Mpc in the line of sight. We take the statistics of these constant redshift 3D simulated boxes as a proxy to the 2D slices at constant redshift that the various telescopes will observe.

3 TOY MODEL FOR THE EVOLUTION OF THE NEUTRAL FIELD

Before delving into the statistics of our four simulated models, we would like to consider a simple toy model for the evolution of the neutral-fraction field's PDF and its associated moments. In the limit that a discrete map be perfectly resolved, a pixel will either be totally neutral or entirely ionized. The PDF for such a field, $P(x_{\text{HI}}|\bar{x}_{\text{HI}}, \text{resolved}, \text{discrete})$, will therefore consist of two weighted Delta-functions δ_{D} . Making use of normalisation and the definition of \bar{x}_{HI} , the PDF is found to be

$$P(x_{\text{HI}}|\bar{x}_{\text{HI}}) = (1 - \bar{x}_{\text{HI}})\delta_{\text{D}}(x_{\text{HI}}) + \bar{x}_{\text{HI}}\delta_{\text{D}}(x_{\text{HI}} - 1), \quad (9)$$

where we have dropped the discrete and resolved conditionals for brevity; this implies that

$$\langle x_{\text{HI}}^n \rangle = \int_0^1 P(x_{\text{HI}}|\bar{x}_{\text{HI}}) x_{\text{HI}}^n dx_{\text{HI}} = \bar{x}_{\text{HI}}. \quad (10)$$

Armed with this PDF we can calculate the evolution of the moments of the neutral fraction as a function of the mean neutral fraction. Using angular brackets to denote volume averaging, we

find for the variance σ^2 , skew S_3 and kurtosis K_4 that

$$\begin{aligned}\sigma^2 &= \langle x_{\text{HI}}^2 \rangle - \bar{x}_{\text{HI}}^2 = \bar{x}_{\text{HI}}(1 - \bar{x}_{\text{HI}}), \\ S_3 &= \langle (x_{\text{HI}} - \bar{x}_{\text{HI}})^3 \rangle \\ &= \bar{x}_{\text{HI}}(1 - \bar{x}_{\text{HI}})(1 - 2\bar{x}_{\text{HI}}) \\ K_4 &= \langle (x_{\text{HI}} - \bar{x}_{\text{HI}})^4 \rangle \\ &= \bar{x}_{\text{HI}}(1 - \bar{x}_{\text{HI}})(3\bar{x}_{\text{HI}}^2 - 3\bar{x}_{\text{HI}} + 1).\end{aligned}\quad (11)$$

These statistics all tend to zero at $\bar{x}_{\text{HI}} = 0$ and $\bar{x}_{\text{HI}} = 1$ as they should, there is also symmetry under $\bar{x}_{\text{HI}} \rightarrow 1 - \bar{x}_{\text{HI}}$.

We plot the analytic moments normalised by σ^n for the n^{th} moment along with that of the x_{HI} maps from our four simulations against the average ionized fraction in Figure 2. In this plot the curves correspond to the toy model (purple stars), global-inside-out (red solid), local-inside-out (blue dot-dashed), global-outside-in (black dotted w/triangles), and local-outside-in (green dashed w/circles). We will use the same model key in all figures hereafter. We see that the local models identically reproduce the distribution of the toy model. This is because these models are constructed without partial ionizations and are for all intents and purposes ‘perfectly resolved’ x_{HI} maps (note that this is not true of the simulated density field used to generate them nor the resulting brightness-temperature maps). Furthermore, it is only in the variance that we see any major deviation of the global models from that of the toy model.

The variance is an inverted parabola where symmetry demands that the maximum be at a mean ionized fraction of 0.5. The skewness displays strong evolution towards the end of reionization (where the average ionized fraction ranges from 0.9 to 1); this feature translates on to the skewness of the brightness-temperature PDF and its potential for use in detecting the end of reionization has been discussed previously (Harker et al. 2009; Ichikawa et al. 2010). The skewness passes from negative values to positive at $\bar{x}_{\text{ion}} = 0.5$; we will see this also propagates onto the brightness-temperature skewness but only for inside-out models. The kurtosis shares the skewness’ strong late-time evolution and also has a perfectly mirrored early-time signature towards the beginning of reionization at mean ionized fraction of between 0 and 0.1. Unfortunately by this point the density field will dominate the statistics and this signature does not translate on to the brightness-temperature maps. This is also the case for the inverted early-time singularity in the skewness, however with inside-out models this produces a detectable early-time minimum as the brightness temperature becomes increasingly influenced by the density field rather than the neutral-fraction field with increasing redshift.

Noting a common factor of σ^2 in all our analytic expressions of equation 11, we plot the central moments of our toy model and simulated x_{HI} maps normalised by σ^2 in Figure 3. This appears to be a slightly more natural normalisation choice with both statistics remaining well behaved, exhibiting no singularities where $\sigma^2 \rightarrow 0$ at either extreme of average ionized fraction. There is a strong deviation at small ionized fractions in the global-outside-in model caused by imperfect resolution coupled to a positive correlation with the density field. This same behaviour is observed in the global-inside-out model but to a lesser extent due to its anti-correlation with the density field.

We conclude that the central moments of the neutral-fraction PDF are essentially model independent, being dominated by the PDF’s bimodal nature and the distribution average. We therefore expect that any model differences discernible by measuring mo-

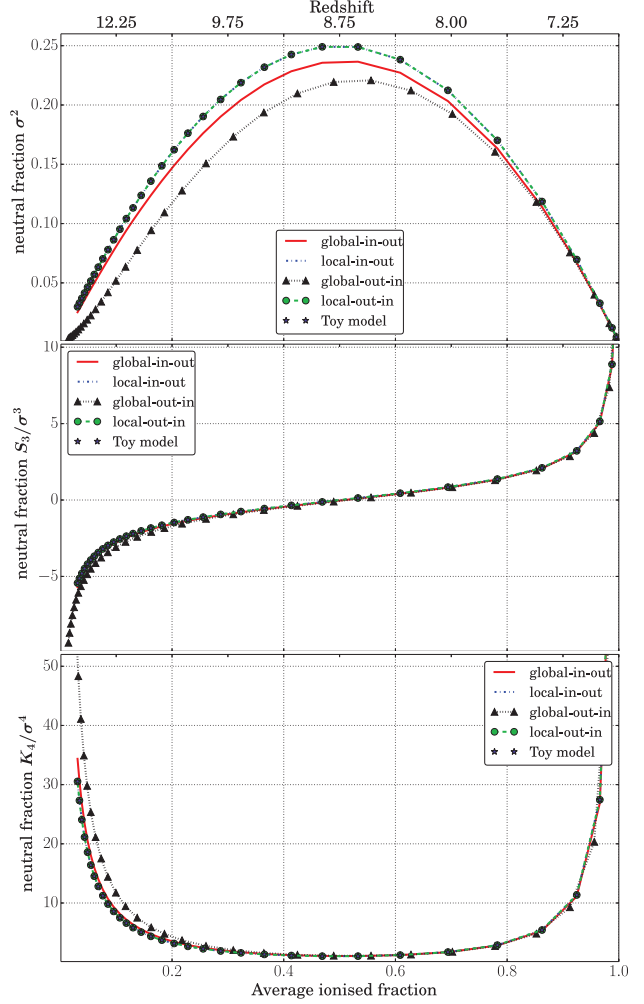


Figure 2. Theoretical prediction for moments of the neutral-fraction PDF and those of the four simulations described in section 2. From top to bottom variance, skewness and kurtosis of the x_{HI} field against $\bar{x}_{\text{ion}} = 1 - \bar{x}_{\text{HI}}$ are plotted. In the simulations the average of a box realisation is taken in calculating the central moments.

ments will result from the relationship between the x_{HI} and density fields. More importantly these signatures offer model independent flags of specific points of the reionization process, namely $\bar{x}_{\text{HI}} > 0.9$, $\bar{x}_{\text{HI}} = 0.5$ and $\bar{x}_{\text{HI}} < 0.1$

4 CLEAN BRIGHTNESS-TEMPERATURE MAPS

Before we consider instrumental noise it is informative to study the brightness-temperature maps from clean simulations. We begin by considering 2D maps from slices of each simulation; Figure 4 shows brightness-temperature maps for each, the depth of each slice is 0.5 Mpc. Maps correspond from top to bottom to: global-in-out, local-inside-out, global-outside-in, local-outside-in and from left to right to $\bar{x}_{\text{ion}} = 0.26$, 0.47 and 0.86 except for global-outside-in which corresponds instead to $\bar{x}_{\text{ion}} = 0.26$, 0.49 and 0.85. The black represents fully ionized regions in which there is no brightness-temperature signal. We see that at higher average ionized fractions the models appear very different. Both local models display a more randomised distribution of smaller islands of signal, with local-outside-in possessing larger ionized regions than

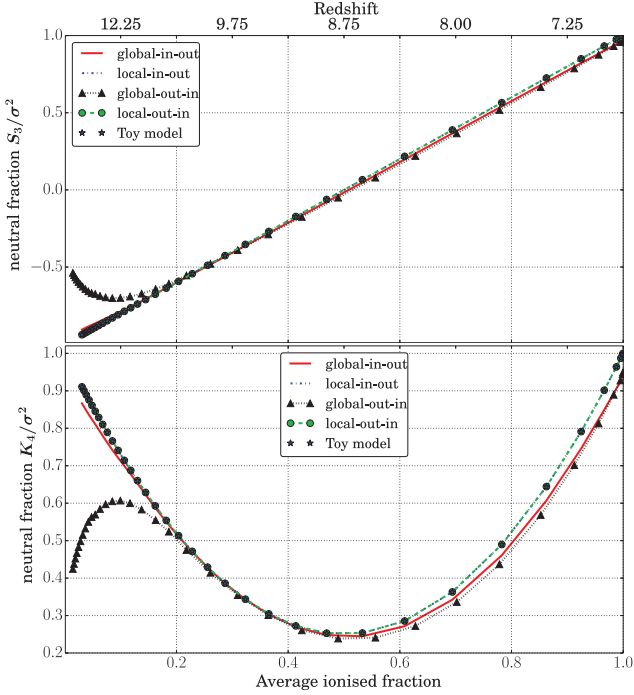


Figure 3. Theoretical prediction for dimensional higher order moments of the neutral-fraction PDF and those of the four simulations described in section 2. From top to bottom we plot the 3rd and 4th central moments each normalised by σ^2 .

that of local-inside-out; this is due to the large voids between the filaments being ionized preferentially in the local-outside-in model. The global models look very different with large cohesive ionized regions dominating the maps. Global-outside-in has smaller cohesive neutral islands than the global-inside-out model, a result of the clustering of matter under gravity into a vast interconnected web. This is easiest to see in the $z = 7.5$ global maps; in the outside-in model the filaments and walls have remained neutral to produce many connected neutral regions. In the inside-out the opposite is true and only the voids remain neutral, resulting in many connected ionized regions around the filaments and walls. Concentrating efforts on imaging the later stages of reionization would be valuable, as at lower mean ionized fractions the ionized bubbles decrease in size and it becomes more difficult to visually differentiate between models.

To quantify this information we calculate the size distributions of the ionized regions in the brightness-temperature maps. We calculate these using the Monte-Carlo method of Mesinger & Furlanetto (2007) in which a random ionized pixel is selected, then the distance to the first ionized-to-neutral transition recorded. This procedure is repeated 10^7 times, from which the size distribution is approximated. The global-outside-in model has slightly smaller bubbles than 21CMFAST for a given average ionized fraction. We therefore identify the average ionized fraction for which global-outside-in appears most like 21CMFAST in terms of bubble size. Size distributions for ionized regions are presented in figure 5; from left to right curves correspond to average ionized fractions of 0.26 (green dashed w/circles), 0.47 (black dotted w/triangles), 0.69 (blue dot-dashed), and 0.86 (red solid) for all but the global-outside-in model which instead corresponds to average ionized fractions of 0.42 (green dashed w/circles), 0.63 (black dotted w/triangles), 0.78 (blue dot-dashed), and 0.91 (red solid). Both local models display

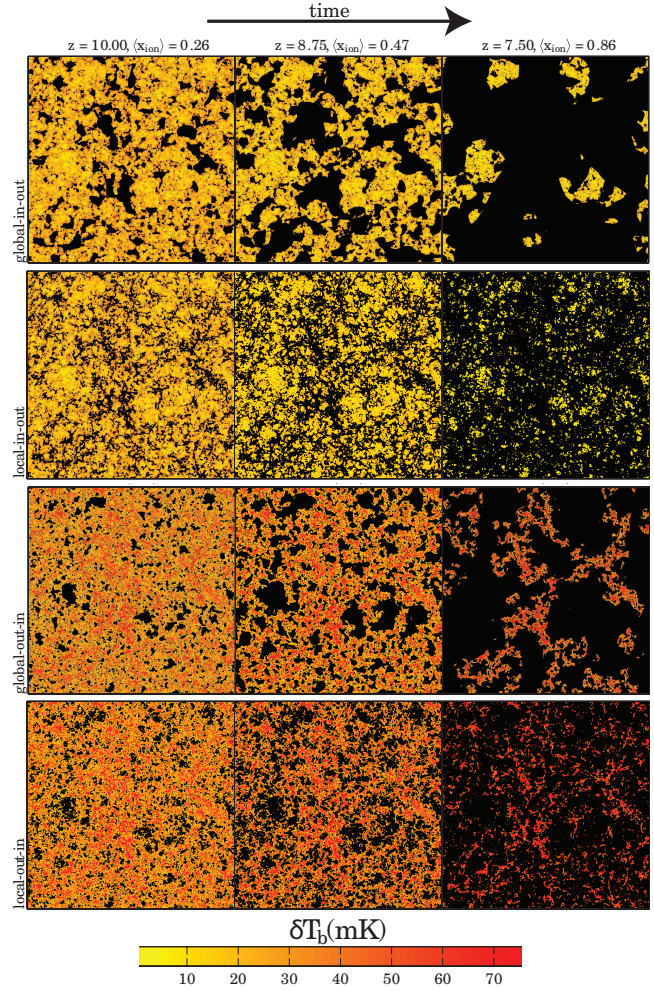


Figure 4. Brightness-temperature maps for 300 Mpc box slices with thickness of 0.5 Mpc. Maps correspond to, from top to bottom: global-in-out, local-in-out, global-out-in, and local-out-in. Panels correspond to $z = 10.00$, $\bar{x}_{\text{ion}} = 0.26$ (left); $z = 8.75$, $\bar{x}_{\text{ion}} = 0.47$ (middle); & $z = 7.50$, $\bar{x}_{\text{ion}} = 0.86$ (right) for all but global outside-in which instead corresponds to, from left to right: $z = 9.75$, 8.75, 7.50 and mean ionized fractions of 0.26, 0.49 and 0.85. Black regions correspond to those that are fully ionized.

very little evolution of size in comparison to the global models. For example, ionized bubble sizes are < 80 Mpc in the local models whereas for the global-inside-out they reach scales of hundreds of Mpc. The global-outside-in develops its larger bubbles later on in the process, but as it is likely that we will not have an absolute measure of the average ionized fraction it will be difficult to distinguish these models by characteristic bubble size alone. Put another way there is degeneracy between the inside-out/ outside-in nature of the model and the timing of reionization when considering the characteristic size of the bubbles.

Plotting the PDF of the brightness-temperature maps, shown in Figure 6 for the global-inside-out model, we see a bimodal distribution as with the neutral-fraction field. Curves correspond to $\bar{x}_{\text{ion}} = 0.26$ (green dashed w/circles), $\bar{x}_{\text{ion}} = 0.47$ (black dotted w/triangles), $\bar{x}_{\text{ion}} = 0.69$ (blue dot-dashed w/diamond) and $\bar{x}_{\text{ion}} = 0.86$ (red solid w/star). Note that the filled symbols at $\delta T_b = 0$ correspond to the fraction of fully ionized pixels rather than their dimensionless probability density. We will not consider

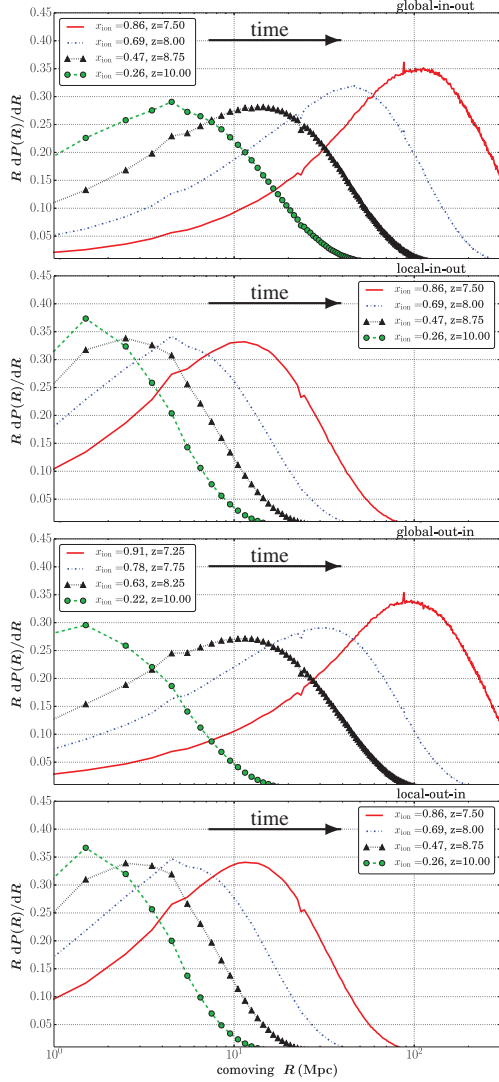


Figure 5. Size distribution of ionized regions $R dP(R)/dR$, where $dP(R)/dR$ is the probability density function for regions of radius R for the four models. Plots correspond to, from top to bottom: global-in-out, local-in-out, global-out-in, and local out-in.

the kurtosis further here, because it will be more difficult to measure and behaves similarly to the skew, dominated by the interplay between the delta function at $x_{\text{HI}} = 0$ and a non-zero distribution.

An important feature that both outside-in models exhibit is considerably higher average temperatures than the inside-out models, where temperatures are boosted by the positive correlation between neutral-fraction and density field. Plotting the average temperature against average ionized fraction in Figure 7 illustrates this point; the outside-in models have average temperatures nearly double that of the inside-out models for a large range of redshifts. From equation 1 we see that neglecting local velocities at a given redshift gives $\langle \delta T_{\text{b}} \rangle \propto \langle x_{\text{HI}} \rangle + \langle x_{\text{HI}} \delta \rangle$, with $\langle x_{\text{HI}} \delta \rangle$ boosting the signal when the neutral fraction and density are positively correlated and suppressing it when this correlation is negative.

As well as 21-cm fluctuation experiments such as those considered here, the epoch of reionization may be constrained by observing the global or average 21-cm brightness temperature signal using single dipole radio telescopes, e.g. Experiment to Detect the Global EoR Signature (EDGES) (Bowman & Rogers 2010;

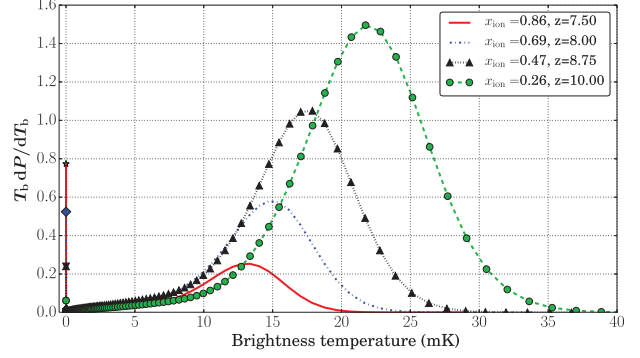


Figure 6. Brightness-temperature PDF from the global-inside-out simulation smoothed on a scale of 1.24 Mpc, where dP/dT_{b} is the brightness temperature probability density. Filled symbols at $\delta T_{\text{b}} = 0$ correspond to the fraction of fully ionized pixels to reduce the contrast between the delta function at $\delta T_{\text{b}} = 0$ and the non-zero distribution.

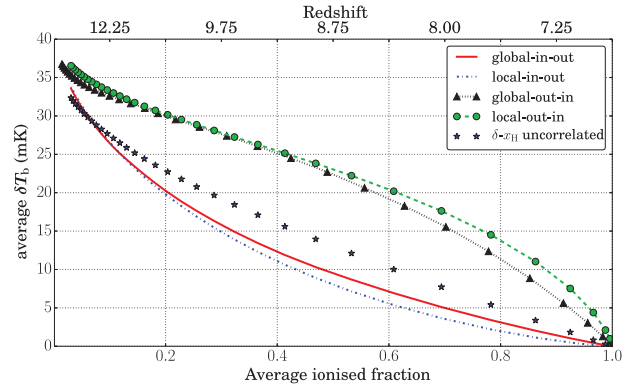


Figure 7. Evolution of average brightness temperature for the four models along with the predicted evolution assuming $\delta \bar{T}_{\text{b}} \propto (1 - \bar{x}_{\text{ion}})$ (purple stars).

Liu et al. 2013). We note that it would be prudent to account for the inside-out/ outside-in nature of reionization when attempting to infer the neutral fraction from the observed average brightness temperature. We see that even the fiducial model exhibits non-negligible deviations from the assumption that $\delta \bar{T}_{\text{b}} \propto (1 - \bar{x}_{\text{ion}})$, plotted with purple stars in Figure 7, by neglecting the anti-correlation between density and neutral-fraction fields. Fortunately, as will be seen in section 5, establishing the inside-out/outside-in nature of reionization should not present a challenge.

5 STATISTICS OF ‘OBSERVED’ BRIGHTNESS-TEMPERATURE MAPS

Until this point we have considered the clean signal and what its statistics tell us about the underlying models. However, this is far from the reality of actually observing these statistics. Any instrument will have a limited observing time (t_{int}) and field of view (FoV); it will observe a range of scales limited by both angular resolution ($\Delta\theta$) and frequency resolution ($\Delta\nu$). Finally, there is instrumental thermal noise to be considered and residuals left after the removal of bright radio foregrounds. The usual approach to foreground removal is to exploit the spectral smoothness of foregrounds; the premise is that foregrounds can be fit, and therefore removed, using a low-order polynomial (McQuinn et al. 2006; Wang

et al. 2006). To further reduce the effects of foregrounds it is possible to exclude from analysis frequency modes in which the foreground residuals are dominant; for example a ‘wedge’ feature exists in the 2D power spectrum in which the contribution from foreground residual noise is confined (Bowman et al. 2009; Datta et al. 2010; Trott et al. 2012).

In this work, we neglect foreground residuals and only consider instrumental effects. We take a simple approach to provide order of magnitude approximations to the noise errors on the various statistics we consider. At the frequencies of relevance, it is reasonable to assume that the system temperature T_{sys} is saturated by the sky temperature and that $T_{\text{sys}} = 180 (\nu/180\text{MHz})^{-2.6}\text{K}$ in quiet portions of the sky (Haslam et al. 1982). The instrumental noise on the brightness temperature, ΔT^N , measured by an interferometer is given by (Furlanetto et al. 2006)

$$\Delta T^N = \frac{T_{\text{sys}}}{\eta_f \sqrt{\Delta \nu t_{\text{int}}}}. \quad (12)$$

Here the array filling factor is defined as $\eta_f = A_{\text{tot}}/D_{\text{max}}^2$, where A_{tot} is the total effective area of the array and D_{max} is the maximum baseline of the array, controlling its resolution.

Throughout we present errors on the fiducial global-inside-out model. In the power spectrum and variance errors are comparable between the different models, but the error on the skewness statistics is much less for the outside-in models although they have a similar qualitative evolution; as such errors on the skewness are pessimistic.

5.1 Power spectrum of noisy maps

To date most attention has been focussed on measuring the power spectrum. As such we will examine the evolution of the power spectrum for our four models before moving on to the moments. The power spectrum is the Fourier transform of the two-point correlation function which measures the level of correlation at different separations in real space. The two-point correlation is defined to be $\xi(\mathbf{r}) = \langle \delta(\mathbf{x})\delta(\mathbf{x}+\mathbf{r}) \rangle$ where the angle brackets denote an average over real space.

We concentrate on the dimensionless power spectrum which we describe using $\Delta_{\delta T_b}^2(k, z) = k^3/(2\pi^2 V) \langle |\delta_{21}(\mathbf{k}, z)|^2 \rangle_k$ in which $\delta_{21} = \delta T_b(\mathbf{k}, z)/\bar{\delta T}_b(z) - 1$, $\bar{\delta T}_b(z)$ is the redshift dependent average brightness temperature calculated from the simulation, V is the volume of the simulated box and the angle brackets denote an average over k -space. By considering only the fluctuating variables in the differential brightness temperature, i.e. $\psi = x_{\text{HI}}(1 + \delta)$, Zaldarriaga et al. (2004) wrote the correlation function as,

$$\xi_\psi = \xi_{xx}(1 + \xi_{\delta\delta}) + \bar{x}_{\text{HI}}^2 \xi_{\delta\delta} + \xi_{x\delta}(2\bar{x}_{\text{HI}} + \xi_{x\delta}). \quad (13)$$

Here we see that the correlation function, and hence the power spectrum, is dependent on the correlation of the neutral-fraction field ζ_{xx} , the correlation function of the density field $\zeta_{\delta\delta}$ and the cross correlation of these two fields $\zeta_{x\delta}$. This expression proves useful when considering the outside-in and inside-out models as their cross-correlation terms possess opposite signs.

To model instrumental errors on the spherically averaged power, we take the approach outlined in the appendix of McQuinn et al. (2006) adopting a logarithmic bin width of $\epsilon = 0.5$. We also assume uniform UV coverage, of which none of the experiments

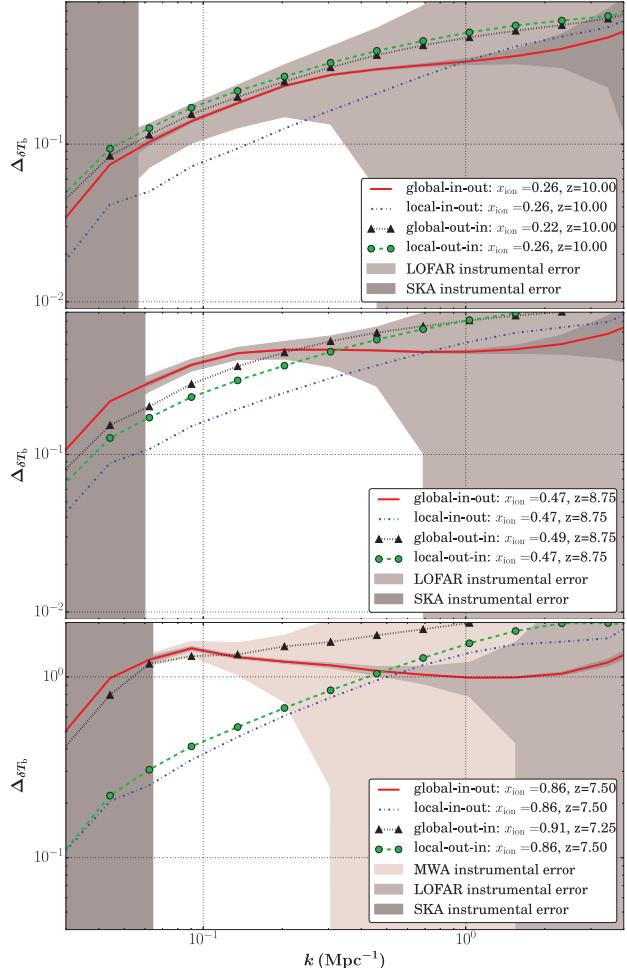


Figure 8. Dimensionless brightness-temperature power spectrum with instrumental errors. Plots correspond to $z = 10.00$, $\bar{x}_{\text{ion}} = 0.26$ (top); $z = 8.75$, $\bar{x}_{\text{ion}} = 0.47$ (middle); and $z = 7.50$, $\bar{x}_{\text{ion}} = 0.86$ (bottom) except for global-outside-in for which we plot the redshift at which the power spectra are most similar. Beige shading depicts the $1\text{-}\sigma$ instrumental errors for the global-inside-out model where light to dark tones correspond to MWA, LOFAR and SKA respectively. The cut off at small k marks the largest scale that the instruments are sensitive to, i.e. $2\pi/D_{\text{max}}$.

we consider can achieve, as such our power spectrum errors are indicative only.

Figure 8 shows errors on the dimensionless brightness temperature power spectrum for the instrumental parameters outlined in Table 2. In this plot, and all those to follow, we use beige shading to depict the $1\text{-}\sigma$ error on a quantity with tone from lightest to darkest corresponding to MWA, LOFAR and SKA respectively. As is evident in this figure, the power spectrum of global-inside-out is strongly sensitive to the characteristic size, with a turnover in the spectrum providing a measure of its scale (Mesinger et al. 2011). Lidz et al. (2008) studied the observational repercussions of this for MWA. They found it possible to constrain the amplitude and slope of the power spectrum for wave-numbers of between $0.1\text{-}1h \text{ Mpc}^{-1}$ and in this decade the amplitude rises and falls during reionization. The slope also flattens out as reionization increases the size of the ionized bubbles. This results from a power boost at this characteristic size, which drops off on larger scales. As expected we see a very similar behaviour in the global-outside-in

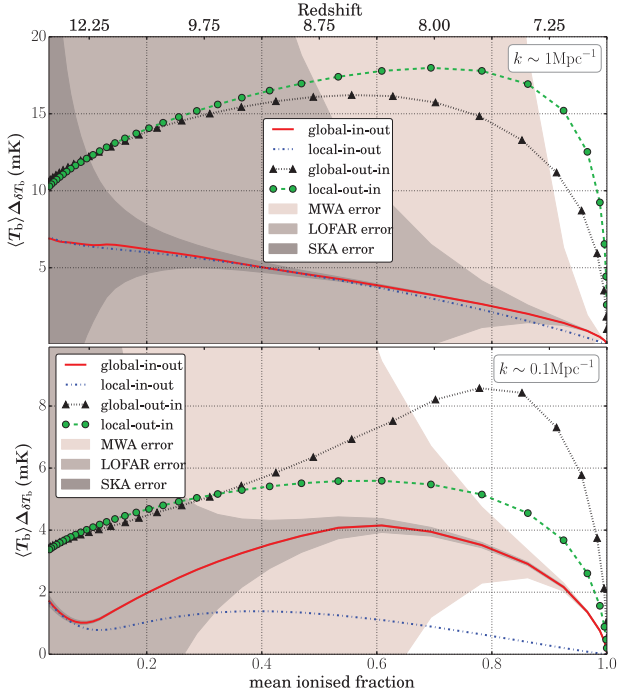


Figure 9. Amplitude of the dimensional brightness-temperature power spectrum as a function of ionized fraction for $k = 1 \text{ Mpc}^{-1}$ (top) and $k = 0.1 \text{ Mpc}^{-1}$ (bottom). Beige shading depict $1\text{-}\sigma$ instrumental errors for the global-inside-out model where light to dark tones correspond to MWA, LOFAR and SKA respectively.

model, however the flattening out of the slope is less pronounced. This is because the positive correlation between δ and x_{HI} boosts the power most at smaller scales. By a mean ionized fraction of roughly 0.5, global-inside-out is the only model to display strong signatures of a characteristic size in the power spectrum, as the additional power on small scales swamps out such a signature in the global-outside-in model. Still, in the absence of a measure of the ionized fraction it will be difficult to know if the power spectrum is dropping rapidly with increasing redshift because reionization’s procession was quick, or because the correct model is global-outside-in. At earlier times/smaller average ionized fraction both outside-in models display more power than the inside-out models due to the positive correlation of x_{HI} and the density field.

If the process of reionization follows a similar timing to that presented here, LOFAR should be able to differentiate global models from the small-scale boost in the global-outside-in model towards the end of reionization, but MWA will not. If the timing of reionization is less favourable and/or foreground residuals boost errors, even just by a bit, then LOFAR too could struggle to distinguish the global models apart to any significance. However, SKA should not have a problem in tightly constraining the models with just the power spectrum.

We plot the evolution of the dimensional power spectrum $\langle \delta T_b \rangle \Delta(k)$ as a function of ionized fraction in Figure 9. The first thing we notice is the higher amplitude of both outside-in models, which can be up to a factor of five greater in outside-in models relative to inside-out models (ignoring comparison between global and local models). This property allows us to easily distinguish between inside-out and outside-in scenarios. We also see that a dramatic rise and fall of the amplitude is common to both global models at $k \sim 0.1 \text{ Mpc}^{-1}$, a feature first noted for the global-inside-out

Table 2. Instrumental specifications assumed for noise calculations. LOFAR and SKA parameters are taken from Mellema et al. (2013) and MWA parameters from Tingay et al. (2013).

Parameter	MWA	LOFAR	SKA
Number of stations (N_{stat})	128	48	450
Effective area ($A_{\text{eff}}/\text{m}^2$)	21.5	804	$10^6/N_{\text{stat}}$
Maximum baseline (D_{max}/m)	2864	3000	10^4
Integration time ($t_{\text{int}}/\text{hours}$)	1000	1000	1000
Bandwidth (B/MHz)	6	6	6

model by Lidz et al. (2008). Interestingly we see similar behaviour in both outside-in models for $k \sim 1 \text{ Mpc}^{-1}$, which occurs because the positive correlation between neutral fraction and small-scale overdensities boosts the reionization mid-phase power, whilst the power is forced to that of the density field at early times and zero at late times. Considering the instrumental errors in Figure 9 we find that MWA should distinguish inside-out from outside-in towards the end of reionization, although not to great significance. LOFAR and SKA should both be able to differentiate between outside-in and inside-out models with the dimensional power spectrum. Both LOFAR and SKA could also potentially constrain the timing of reionization using the global model’s mid-phase maximum in the amplitude of the dimensional power spectrum at $k \sim 0.1 \text{ Mpc}^{-1}$ (or $k \sim 1 \text{ Mpc}^{-1}$ if global-outside-in transpires to be the correct model).

5.2 Moments of noisy maps

For the estimate of noise induced error on the moments we assume that there is independent noise in each pixel and that this noise is well described by a Gaussian random error with zero mean and standard deviation σ_{noise} derived from equation 12 to be,

$$\sigma_{\text{noise}}^2 = 2.9 \text{mK} \left(\frac{10^5 \text{m}^2}{A_{\text{tot}}} \right) \left(\frac{10'}{\Delta\theta} \right)^2 \times \left(\frac{1+z}{10.0} \right)^{4.6} \sqrt{\left(\frac{1 \text{MHz}}{\Delta\nu} \frac{100 \text{hours}}{t_{\text{int}}} \right)}. \quad (14)$$

To derive this expression we have made use of the relation $D_{\text{max}} = \lambda/\Delta\theta$.

We assume the instrumental parameters of table 2 in working out the pixel noise properties. We fix the pixel size for the sake of computational efficiency to $R_{\text{pix}} = 6 \text{ Mpc}$ and $R_{\text{pix}} = 2 \text{ Mpc}$ to match the resolution of MWA/LOFAR and SKA respectively. We then proceed to smooth and re-sample the simulation boxes according to these pixel sizes and recalculate each statistic from these ‘observed’ boxes. We fix the angular resolution by the ‘observed’ pixel size R_{pix} of our simulation. These radio telescopes will have far better resolution in the frequency direction, but we bin to improve signal to noise by matching the frequency resolution to simulation pixel size, i.e. $\Delta\nu = H_0 \nu_0 \sqrt{\Omega_m} R_{\text{pix}} / [c \sqrt{(1+z)}]$.

The method for propagating the instrumental noise of equation 14 on to errors on the moments are detailed in the appendix. In short, we assume each pixel has a measured signal associated with it $x_i = \delta T_i + n_i$, where δT_i is the true signal in the pixel and the noise on the pixel n_i obeys the properties outlined at the start of

this section. In this picture, we imagine that the simulation boxes represent some true measurable signal and we take central moments relative to the mean of the box $\delta\bar{T}_b = N_{\text{pix}}^{-1} \sum_{i=0}^{N_{\text{pix}}} \delta T_i$. The true moments in which we are interested are

$$\begin{aligned} S_2 &= \frac{1}{N_{\text{pix}}} \sum_{i=0}^{N_{\text{pix}}} [\delta T_i - \delta\bar{T}_b]^2, \\ S_3 &= \frac{1}{N_{\text{pix}}} \sum_{i=0}^{N_{\text{pix}}} [\delta T_i - \delta\bar{T}_b]^3, \\ K_4 &= \frac{1}{N_{\text{pix}}} \sum_{i=0}^{N_{\text{pix}}} [\delta T_i - \delta\bar{T}_b]^4, \end{aligned} \quad (15)$$

which correspond to the variance, skew and kurtosis respectively. We construct a test statistic for the m^{th} moment according to $N_{\text{pix}}^{-1} \sum_{i=0}^{N_{\text{pix}}} (x_i - \bar{x}_i)^m$. Averaging this test statistic over noise realisations, we would expect to recover the true statistic if it was unbiased, any surplus is the bias of the test statistic and can be used to construct an unbiased statistic. We found the skew test statistic to be unbiased, but that the naive test estimator for the variance does suffer from bias. This bias is removed by instead using

$$\hat{S}_2 = \frac{1}{N_{\text{pix}}} \sum_{i=0}^{N_{\text{pix}}} (x_i - \bar{x})^2 - \sigma_{\text{noise}}^2. \quad (16)$$

The variance of each estimator can then be calculated and propagated on to the error on to $\gamma_3 = \hat{S}_3/\hat{S}_2$ and $\gamma'_3 = \hat{S}_3/(\hat{S}_2)^{3/2}$ to give

$$\begin{aligned} V_{\hat{S}_2} &= \frac{2}{N} (2S_2\sigma_{\text{noise}}^2 + \sigma_{\text{noise}}^4), \\ V_{\gamma_3} &\approx \frac{1}{(S_2)^2} V_{\hat{S}_3} + \frac{(S_3)^2}{(S_2)^4} V_{\hat{S}_2} - 2 \frac{S_3}{(S_2)^3} C_{S_2 S_3}, \\ V_{\gamma'_3} &\approx \frac{1}{(S_2)^3} V_{\hat{S}_3} + \frac{9}{4} \frac{(S_3)^2}{(S_2)^5} V_{\hat{S}_2} - 3 \frac{S_3}{S_2^4} C_{\hat{S}_2 \hat{S}_3}, \end{aligned} \quad (17)$$

where

$$V_{\hat{S}_3} = \frac{3}{N_{\text{pix}}} (3\sigma_{\text{noise}}^2 K_4 + 12S_2\sigma_{\text{noise}}^4 + 5\sigma_{\text{noise}}^6), \quad (18)$$

and

$$C_{\hat{S}_2 \hat{S}_3} = \frac{6}{N_{\text{pix}}} S_3 \sigma_{\text{noise}}^2. \quad (19)$$

There is a further subtlety in that the value of N corresponds to the number of pixels that the full FoV for each telescope would measure rather than the number of pixels in a simulated box. We must then work out the number of pixels that would fit into a single FoV. We assume a frequency depth or bandwidth $B = 6$ MHz over which the evolution in the brightness temperature is negligible; the number of pixels measured is then taken to be $N = (L_{\text{FoV}}/R_{\text{pix}})^2 (B/\Delta\nu)$, for which we approximate the FoV as a square of side L_{FoV} .

5.3 Variance

The variance is intimately related to the power spectrum; it is the zero separation two-point correlation function $\xi(0)$, which is equivalent to an integral over the power spectrum of fluctuations,

i.e.

$$\begin{aligned} \xi(\mathbf{r}) &= \int P(\mathbf{k}) \exp(i\mathbf{k} \cdot \mathbf{r}) \frac{d^3\mathbf{k}}{(2\pi)^3}, \\ \xi(0) &= \sigma^2 = \int P(\mathbf{k}) \frac{d^3\mathbf{k}}{(2\pi)^3}. \end{aligned} \quad (20)$$

Whilst the variance does not offer any fundamentally new information, the simplicity of this statistic will make it easier to measure and interpret. Furthermore instrumental effects are expected to affect statistics measured from maps differently than they will the power spectrum (Petrovic & Oh 2011). We calculate the variance in the δT_b maps according to

$$\sigma^2 = \frac{1}{N_{\text{pix}}} \sum_i^{N_{\text{pix}}} [\delta T_i - \delta\bar{T}_b]^2, \quad (21)$$

here N_{pix} is the total number of pixels in the simulated box, δT_i is the differential brightness temperature in the i^{th} pixel and $\delta\bar{T}_b = N_{\text{pix}}^{-1} \sum_i^{N_{\text{pix}}} \delta T_i$ is the average in the simulated box. The evolution of this variance with average ionized fraction is shown in the bottom plot of Figure 10.

We note that discretization effects of the density field induced when modelling of peculiar velocities were found to propagate onto the brightness-temperature PDF, affecting the evolution of the moments; this effect is particularly pronounced at early times when the density-field's statistics dominates the signal. We find that re-sampling to a resolution of 150 resolves the discretization issue, this produces pixels of side 2 Mpc, the kind of resolution expected from SKA. As a rule of thumb we find it sufficient to resample to one quarter of a simulation's original resolution.

As expected, the variance shows little sensitivity to global or local nature, there are however strong differences in evolution between the inside-out models and the outside-in. It is therefore extremely useful for distinguishing between these types of model. These differences are due to the much higher brightness temperatures of outside-in models producing larger variance between the regions of lowest or highest temperature and the map average. We conclude that observing very high variance would be indicative of an outside-in scenario. The higher variance of outside-in models was qualitatively noted by Furlanetto et al. (2004) when considering the brightness-temperature PDF during reionization.

If we consider the limits of this evolution, we see that once reionization is complete there can be no signal; at the other extreme, where it has yet to commence, the variance of the brightness temperature will be entirely defined by that of the density field. As a result we observe an inverted parabola that peaks around the half way point for all models but local-inside-out. The peak is shifted right in the outside-in models where the variance is boosted until later because of the positive correlation between the density and the neutral-fraction fields producing a more extreme non-zero distribution.

LOFAR, whose errors are shown in Figure 10 (top), should not be limited by instrumental noise in detecting the variance providing that nature has been kind with the timing of reionization. LOFAR will certainly be able to exclude the outside-in models provided our observations that reionization was drawing to a close at $z \sim 7$ are borne out. We find that the current planned configuration for MWA will not be able to overcome thermal noise in order to observe the variance with resolution ~ 6 Mpc. SKA on the other hand is expected to achieve small errors on the variance at most of

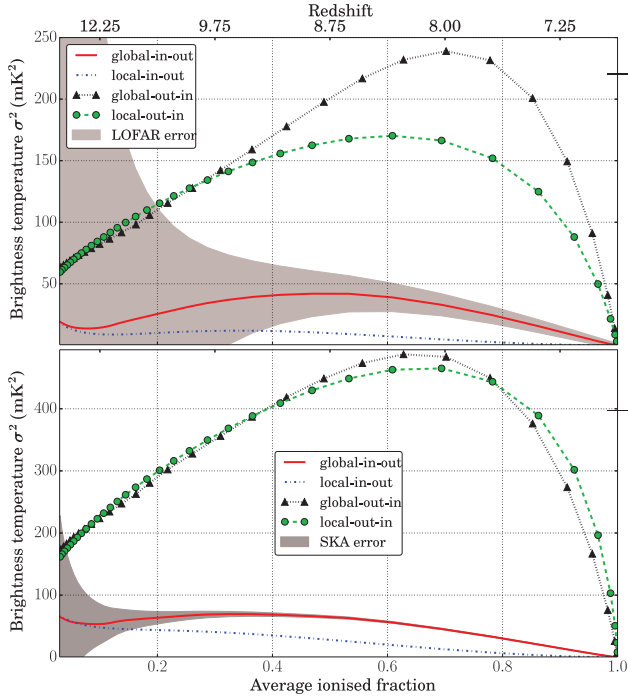


Figure 10. Variance of brightness temperature as measured in ‘observed’ maps with a co-moving pixel size of 6 Mpc for LOFAR (top) and 2 Mpc for SKA (bottom), taken to be reflective of each instrument’s resolution. Beige shading depicts $1\text{-}\sigma$ instrumental errors for the global-inside-out model.

the redshift range we have considered. As it is unlikely that reionization will have ended earlier than this, we conclude that there is great potential for distinguishing between models by measuring the variance with the SKA. We find all instruments to be better at constraining models and timing using the dimensional power spectrum rather than the variance at the default resolution we have considered in this section.

5.4 Skewness

As the variance is connected to the power spectrum so too is the skew to the bi-spectrum. The bi-spectrum is the Fourier transform of the 3-point correlation $\zeta(\mathbf{r}_1, \mathbf{r}_2) = \langle \delta(\mathbf{x})\delta(\mathbf{x} + \mathbf{r}_1)\delta(\mathbf{x} + \mathbf{r}_2) \rangle$, where the angle brackets denote an average over real space or realisations; this measures the correlation between 3 points in real space. The skew is then equal to $\zeta(0, 0)$, the zero separation 3-point correlation function. The bi-spectrum is beyond the scope of this paper but will be looked at in future work. Once reionization commences the brightness-temperature field becomes extremely non-Gaussian (as seen in the PDF of Figure 6) and so it becomes necessary to consider higher order statistics than the power spectrum. The skew is therefore a very valuable statistic for teasing out information beyond that contained in 2-point statistics, without the complexity of bi-spectrum measurements.

We consider the normalised third moment of the full brightness-temperature maps S_3/σ^3 (the skewness) where,

$$S_3 = \frac{1}{N_{\text{pix}}} \sum_i^{N_{\text{pix}}} [\delta T_i - \delta \bar{T}_b]^3, \quad (22)$$

N_{pix} is the total number of pixels in the map, δT_i is the differ-

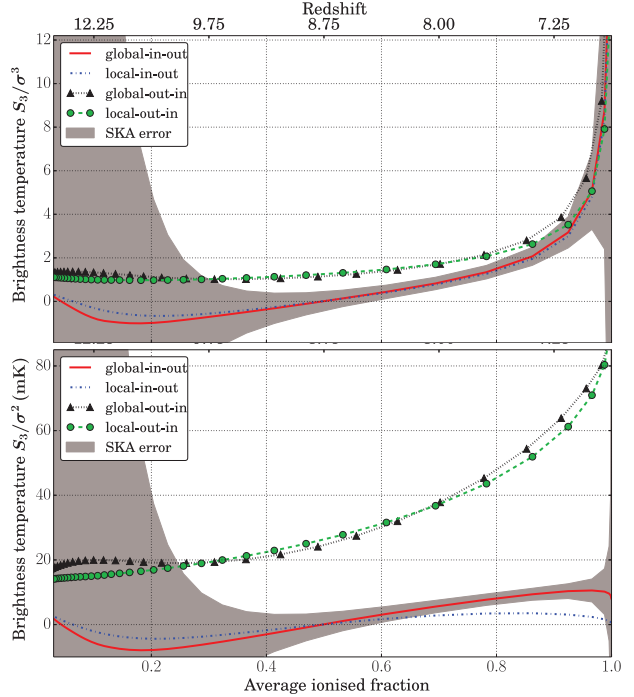


Figure 11. Skewness (top) and dimensional skewness (bottom) of the brightness temperature as measured in ‘observed’ maps against average ionized fraction. Beige shading depicts $1\text{-}\sigma$ instrumental errors for the global-inside-out model. Simulations are smoothed and re-sampled to reflect the default resolution of SKA, i.e. pixels of side 2 Mpc.

tial brightness temperature of the i^{th} pixel and $\delta \bar{T}_b$ is the average temperature in the box.

Figure 11 (top) shows the skewness evolution for the four models. As with the skewness of the neutral field we see a sharp increase at the end of reionization, i.e. $\bar{x}_{\text{ion}} > 0.9$; again this feature is found to be largely model independent, being strongly dominated by an increasing delta function at $\delta T_b = 0$.

As for distinguishing between models, we see differences up until $\bar{x}_{\text{ion}} \sim 0.9$. These differences are slight, with the inside-out model’s larger skewness originating in the positive $\delta\text{-}x_{\text{HI}}$ correlation. Inspired by our analytical expressions for the moments of the neutral-fraction PDF we plot the dimensional skewness S_3/σ^2 in Figure 11 (bottom). We see that the inside-out and outside-in models exhibit markedly different evolution of the dimensional skewness. At early times inside-out models decrease with ionized fraction whereas outside-in increase; during the mid-phases all display increasing dimensional skewness, then at later times the inside-out models drop off whilst the outside-in models increase in an almost exponential fashion. It is useful to refer back to the dimensional skewness of the neutral fraction (Figure 3), we see that positive correlation between neutral fraction and density in the outside-in models serve to accentuate the features of the neutral-fraction field. In inside-out models this behaviour is ultimately suppressed as high density regions are ionized over low density regions reducing the higher-temperature tail of the non-zero part of the PDF. Whilst strong model differences exist, we do already have a means to constrain this behaviour in the variance. However, the dimensional skewness’ model differences are very strong right up until the end of reionization, where as they are reduced in the variance as it is rapidly dropping off during this phase.

The potential for the observing the skew on initial inspection

seems less promising than for the variance; the noise dominates the skew entirely for LOFAR and MWA. However for SKA the sharp increase signifying the end phase of reionization should not be noise dominated, this is illustrated top plot of Figure 11 which shows the evolution of skewness with $1\text{-}\sigma$ SKA instrumental errors. The suppression of variance in the maps alters the evolution of the skewness. In the inside-out model this results in an evolution much closer to that of the neutral-fraction maps, being drawn to negative values as the skewness becomes increasingly influenced by the neutral-fraction field at early times such that a minimum is exhibited around $\bar{x}_{\text{ion}} \sim 0.2$, then during the mid-phase it passes from negative to positive. The evolution of the dimensional skewness S_3/σ^2 is presented in the bottom plot of Figure 11; suppression of the variance from smoothing the maps accentuates the features of this statistic. This is particularly valuable for identifying inside-out reionization which exhibits strong negative values during the early stages of reionization and passes from negative to positive at the mid-phase again echoing the evolution of the neutral-fraction’s dimensional skewness. This provides potentially useful signatures in the early minimum, mid-phase transition from positive to negative, and late-time maximum in the global-inside-out’s dimensional skewness. Whilst the skewness already provides us with such a late-time signature its similar early-time minimum is much weaker and may be harder to definitively detect. However, from the $1\text{-}\sigma$ errors in Figure 11 it is clear that SKA will not be able to constrain the dimensional skewness very well with 2 Mpc pixels.

5.5 Smoothing ‘observed’ maps to reduce noise

It was noted by Harker et al. (2009) that smoothing their residual maps improved LOFAR’s ability to constrain the skewness, something we find it unable to do at a resolution of 6 Mpc. We therefore investigate the effect of further smoothing and re-sampling the ‘observed’ brightness-temperature maps to increase pixel size and hence reduce pixel noise.

We find the model differences observed in the brightness-temperature variance to be very robust to smoothing, although naturally its magnitude reduces with increased smoothing. As one might expect, smoothing most aggressively suppresses the variance at early and late times, when the field is Gaussian (early-times) or sparsely populated (late-times). The mid-point maximum in inside-out models remains robustly at $0.5 \leq \bar{x}_{\text{ion}} \leq 0.6$ up to smoothing scales of $R_{\text{smooth}} = 60$ Mpc, the largest smoothing scale we consider. Although the local-inside-out’s signal is smoothed out at much smaller smoothing scales than this as it has much lower variance than the other models; its early eradication under smoothing compared to the other models is a signature of this. For global-outside-in, the mid-phase maximum shifts to higher \bar{x}_{ion} with increased smoothing and so care would have to be taken in its interpretation under smoothing. These differences in behaviour under increasing degrees of smoothing offer another method to differentiate between the four models we consider.

In both global models the late-time increase in the skewness is robust up to smoothing scales of $R_{\text{smooth}} \sim 50$ Mpc beyond which it becomes too damped to contrast the $\bar{x}_{\text{ion}} < 0.1$ evolution sufficiently. This signature is wiped out from the local models at smoothing scales of $R_{\text{smooth}} \sim 20$ Mpc and beyond. The early-time turnover in the global-inside-out model is wiped out much beyond $R_{\text{smooth}} \sim 20$ Mpc, however it is robustly located at $\bar{x}_{\text{ion}} \sim 0.2$ at lower smoothing scales. Whilst the qualitative behaviour of the dimensional skewness is robust to smooth-

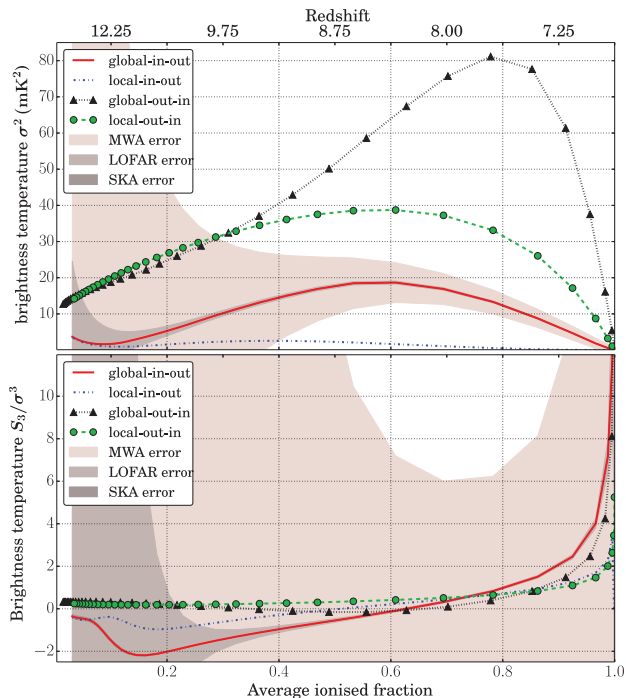


Figure 12. Brightness-temperature variance (top) and skewness (bottom) as measured in ‘observed’ maps smoothed on scales of $R_{\text{smooth}} = 10$ Mpc against average ionized fraction. Beige shading depicts $1\text{-}\sigma$ instrumental errors on the global-inside-out model; light to dark tones correspond to MWA, LOFAR and SKA errors respectively.

ing, the early and late-time vertices become washed out beyond $R_{\text{smooth}} \sim 15$ Mpc.

We present the variance of ‘observed’ maps smoothed with a smoothing radius of $R_{\text{smooth}} = 10$ Mpc in the top plot of Figure 12, this illustrates that such smoothing allows LOFAR to constrain the variance tightly out to $z \sim 12$ and renders SKA errors negligible for the entire redshift range we consider. Whilst MWA’s performance is not outstanding we find that smoothing the maps up to $R_{\text{smooth}} = 30$ Mpc or more allows MWA to better constrain the outside-in/ inside-out nature of our models using the variance than it can with the dimensional power spectrum; we find this to be the case even for smoothing of half this scale.

The bottom plot shows the skewness in maps again smoothed to $R_{\text{smooth}} = 10$ Mpc. At this smoothing scale LOFAR will tightly constrain the skew up to $z \sim 10$ and SKA’s errors are rendered negligible. Both LOFAR and SKA will be able to differentiate between models using the skewness; in particular any detection of negative skewness would be indicative of an inside-out model for reionization and $\bar{x}_{\text{ion}} < 0.6$ at the given redshift. The mid-phase crossing from negative to positive will also be possible to constrain although we note that it drifts to $\bar{x}_{\text{ion}} \sim 0.6$ with smoothing. Furthermore, at this smoothing scale SKA is sensitive to the early-time $\bar{x}_{\text{ion}} \sim 0.2$ minimum in the skewness of global-inside-out. Constraints of the early and mid-phase signatures will be even stronger using the dimensional skewness which has comparable errors to that of the skewness on this smoothing scale. LOFAR will also be able to constrain this statistic until $z \sim 10$ at this smoothing scale, and in doing so could constrain reionization’s timing by the detection or absence of the early-time minimum and mid-phase transition from negative to positive. Again if the observed maps are smoothed to scales of $R_{\text{smooth}} = 30$ Mpc, MWA is able to con-

strain the both skewness statistics up to $z \sim 9$. It is worth noting that we also looked at the performance of the proposed instrument HERA (Pober et al., 2013) and find its constraints on the variance to be almost as tight as those of SKA; HERA would also improve constraints on the skewness, pushing back sensitivity by $\Delta z \sim 2$ as compared to LOFAR constraints.

6 COSMIC VARIANCE IN NOISE-FREE MAPS

A box of 300 Mpc on a side is a large sample and we expect this to be representative of the Universe’s total density field. However the process of reionization is extremely non Gaussian and so we expect measurements of the brightness temperature to suffer more extremely from cosmic variance, especially at the later stages when regions of neutral hydrogen will be increasingly rare. Another aspect of this is that our simulation essentially follows one region of the Universe over a range of redshift; our measurements will come from independent regions of the Universe at different redshifts. These different regions of the Universe will each have statistics that differ from each other and that of the full sample. We attempt to gain some insight of this effect by using our simulation as a proxy for the full sample (the Universe) and take sub-samples from our proxy to see how much each statistic varies. Of course, this gives us no insight into how our simulation is biased from the full distribution; to estimate this would require repeat samples with different initial conditions, a less practical option given the scale of our simulation. There is also the issue that our sub-samples are smaller than our simulation box and so will suffer from a larger cosmic variance. Even our simulation box size is different from the instrument FoVs; for example the ratio of sub-sample volume to instrumental volume is 0.003, 0.01 and 0.02 for MWA, LOFAR and SKA respectively at a redshift of 8.5. It is clear then that our estimate of cosmic variance will be larger than the true cosmic variance that the three experiments we consider will have to contend with. As such we take our estimates as an upper-bound and use them for qualitative insight to the way the statistics will be affected.

We break our simulation box into 8 sub-samples of side 150 Mpc and calculate the variance and skew statistics for each individual sub-sample. Each statistic’s variance relative to that of the sub-sample population’s mean is then calculated. We note that the sub-sample population mean of each statistic is biased relative to that of the full-box due to the small sub-sample box size; this has been studied at length by Iliev et al. (2013) from which we can conclude that our full box should not be biased in such a way.

The cosmic variance induced $1\text{-}\sigma$ errors for the variance (top), skewness (middle) and dimensional skewness (bottom) are presented in Figure 13. Cosmic variance should not pose any barrier in detecting the variance of the brightness temperature. If it transpires that global-outside-in best describes the nature of reionization then the cosmic variance error could be as big as 180 mK during the mid-phases. Of course the variance evolution is much more dramatic in outside-in models and so the conclusion that cosmic variance will not cause problems in measuring the variance holds. Cosmic variance will however impact detection of the skewness at late times, but it should be possible to detect an increase in skewness towards the end of reionization. The late-time maximum in the evolution of dimensional skewness might not be evident, but the early-time equivalent in the inside-out models will be measurable. Combined with the late-time rapid increase in skewness, its mid-phase transition to negative skewness and a corresponding maximum in the

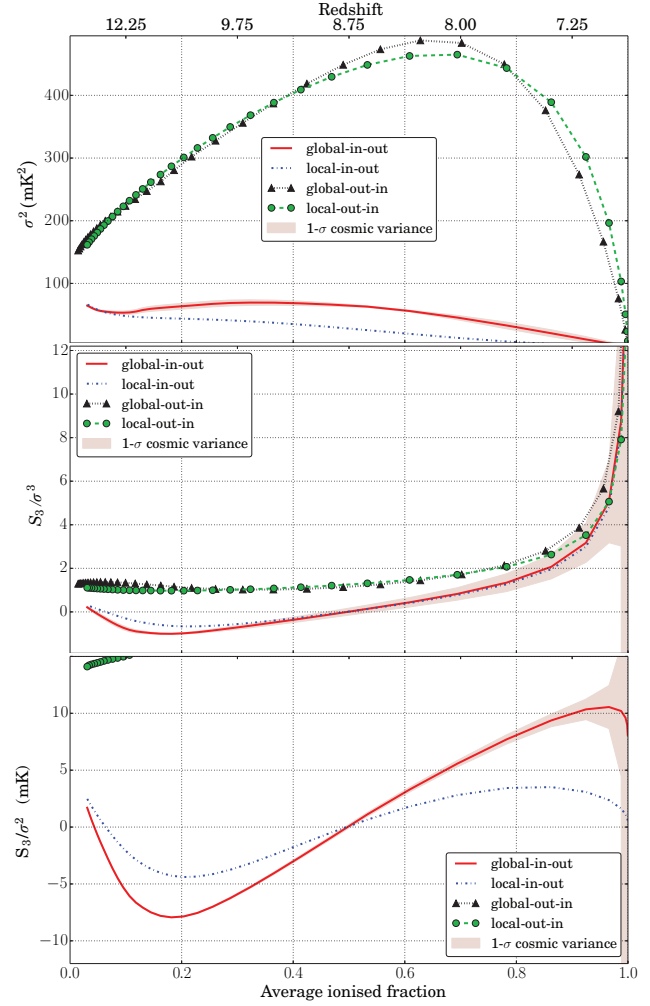


Figure 13. Cosmic variance induced errors as estimated from sub-sampling our full box into 2^3 boxes of side 150 Mpc, then calculating the sub-sample variance relative to the statistics of the full box for the brightness-temperature variance (top), skewness (middle) and dimensional skewness (bottom). Beige shading depicts $1\text{-}\sigma$ cosmic variance error on the global-inside-out model.

variance we have detectable signatures of three distinct phases in the process of reionization.

7 CONCLUSIONS

In this paper a set of reionization simulations have been built upon our reference model 21CMFAST, an efficient semi-numerical simulation that is representative of our present understanding of the likely nature of reionization. Our four models are: 21CMFAST, a global-inside-out model in which large ionized bubbles grow around large-scale overdensities; global-outside-in, where large ionized bubbles grow around large-scale underdensities; local-inside-out, where small bubbles are located in over-dense regions; and local-outside-in, with small bubbles in under-dense regions. We apply this testing set to the power spectrum and the moments of the 21-cm brightness temperature 1-point distribution to tease out how these statistics are influenced by the general properties we model, i.e. large or small bubbles located in under or over-dense regions. We then consider the effect of instrumental noise and discuss the

practicalities of actually distinguishing between models using observations from the three main radio telescopes that aim to measure the 21-cm fluctuations during reionization, namely MWA, LOFAR and SKA. We then consider the challenge that the variability arising from only measuring limited regions of the Universe rather than the full Universe presents to interpreting observations with moments of brightness-temperature maps.

Outside-in models possess higher brightness temperatures than inside-out models due to the positive correlation between density and neutral-fraction; this boosts the variance and power spectrum accordingly. The evolution of the average brightness temperature in maps is found to be nearly double in outside-in models; this must be accounted for when inferring the neutral fraction from average brightness-temperature measurements from global 21-cm surveys. We find the variance to be the best option for distinguishing the outside-in/inside-out nature of reionization; by smoothing noise out over 10 Mpc or greater even the pre-SKA telescopes will be able to achieve this out to redshifts of 12 (LOFAR) and 10 (MWA). The detection of negative skewness is strongly indicative of reionization being inside-out in nature, the evolution of the dimensional skewness is also very different in outside-in models, rising much more aggressively during reionization. Again, with the help of smoothing, pre-SKA instruments could exploit these differences in out to redshifts of 10 (LOFAR) and 9 (MWA).

The moments primarily depend on the density to neutral-fraction correlation. As such it is only really the power spectrum that offers a means to constraining the global/local nature of reionization. The power spectrum show strong rise and fall in amplitude at scales of $k \sim 0.1$ for both global models where power is boosted by a large characteristic ionized bubble size. It should be possible to use this signature, unique to global models, to exclude local models even with pre-SKA instruments. However, low sensitivity to the power spectrum may prevent the pre-SKA instruments from distinguishing global-outside-in models from global-inside-out, both of which exhibit a turnover at the scales of their characteristic bubbles. The degeneracy between the power spectrum's evolution with redshift and the global-outside-in/inside-out nature complicates their separation further. SKA should be able to use the power boost in outside-in models, evident at small scales late in the reionization process and at all scales earlier on, to distinguish these two models.

So long as reionization does progress in a global-inside-out manner, there will exist signatures of specific points of the reionization epoch in the variance and skewness, all of which should be exploitable by pre-SKA instruments. A minimum at $\bar{x}_{\text{ion}} \sim 0.2$ is evident in both skewness and dimensional skewness; both then transition from negative to positive at $\bar{x}_{\text{ion}} \sim 0.5$ and the variance reaches its maximum around this same time; finally the skewness rises rapidly at $\bar{x}_{\text{ion}} > 0.9$. Cosmic variance may make the late-time signature in the skewness more of a challenge to detect, but should not suppress its observation entirely.

There are of course several caveats to this work. We present a single model for the evolution of the neutral fraction with redshift, as such, reionization events described here are likely to be shifted in redshift. This evolution was chosen to present a best case scenario, our findings for instrumental effects are therefore optimistic. Our error treatment ignores correlations in noise between pixels and therefore provides only order of magnitude error estimates. Whilst such correlations are important, their effects are likely to be negligible in comparison to error induced by foreground residuals, which we make no attempt to incorporate in this work. Neglecting foregrounds allows for clean interpretation of the underlying statistics and understanding of instrumental effects. We have only made a

simple estimate of cosmic variance, but this is sufficient to show it should not seriously hamper efforts to constrain reionization with the 21-cm line. Detailed modelling of the spatial distribution of array stations should be incorporated in future work, but our modelling, whilst simplistic, is sufficient to estimate the errors. Most of the characteristics we have considered appear robust to smoothing so it is the hope that this would also be the case with incomplete sampling; however, this should be investigated in full. Finally, we have neglected spin temperature fluctuations; if X-ray heating is very delayed compared to that considered here, then a large contrast between a very cool neutral IGM and ionized regions could produce a variance evolution comparable to that of the outside-in models (Pritchard & Furlanetto 2007; Mesinger, Ewall-Wice & Hewitt 2013).

Four simple models for reionization have been explored, showing that moments of the PDF show certain information complementary to that of the power spectrum. We find that pre-SKA instruments may struggle in distinguishing between global-inside-out and global-outside-in from the power spectrum alone but that they will be well placed to break this degeneracy by measuring the variance. Signatures of the early, mid and late phases of reionization exhibited by the variance and skewness should be detectable at a wide range of redshift with the pre-SKA instruments considered. The early and mid phase signatures are more pronounced in the dimensional skewness, this statistic may therefore prove more robust to foreground residuals. We conclude that whilst efforts to date have put great emphasis on measuring the power spectrum, in the future, more focus must be placed on measuring the moments, whose simplicity make them much more accessible in the short term.

ACKNOWLEDGEMENTS

The authors would like to thank Daniel Mortlock and Andrew Jaffe for useful discussions and suggestions. We also thank Andrei Mesinger for making the 21CMFAST code used in this paper publicly available. CW is supported by an STFC studentship. JRP acknowledges support under FP7-PEOPLE-2012-CIG grant #321933-21ALPHA and STFC consolidated grant ST/K001051/1.

REFERENCES

- Alvarez M. A., Abel T., 2012, ApJ, 747, 126, arXiv:1003.6132
- Barkana R., Loeb A., 2001, Phys. Rep., 349, 125, arXiv:astro-ph/0010468v3
- Barkana R., Loeb A., 2008, MNRAS, 384, 1069, arXiv:0705.3246
- Becker R. H. et al., 2001, AJ, 122, 2850, arXiv:astro-ph/0108097
- Bennett C. L. et al., 2013, ApJS, 208, 20, arXiv:1221.5225
- Bittner J. M., Loeb A., 2011, J. Cosmology & Astroparticle Phys., 2011, 38, arXiv:1006.5460
- Bolton J. S., Becker G. D., Wyithe J. S. B., Haehnelt M. G., Sargent W. L. W., 2010, MNRAS, 406, 612, arXiv:1001.3415
- Bolton J. S., Haehnelt M. G., Warren S. J., Hewett P. C., Mortlock D. J., Venemans B. P., McMahon R. G., Simpson C., 2011, MNRAS: Letters, 416, L70, arXiv:1106.6089
- Bond J. R., Cole S., Efstathiou G., Kaiser N., 1991, ApJ, 379, 440
- Bowman J. D., Rogers A. E., 2010, Nature, 468, 796
- Bowman J. D., Morales M. F., Hewitt J. N., 2009, ApJ, 695, 183, arXiv:0807.3956

- Choudhury T. R., Ferrara A., Gallerani S., 2008, *MNRAS: Letters*, 385, L58
- Crociani D., Mesinger A., Moscardini L., Furlanetto S., 2010, *MNRAS*, 411, 13, arXiv:1008.0003
- Datta A., Bowman J. D., Carilli C. L., 2010, *ApJ*, 724, 526, arXiv:1005.4071
- Dijkstra M., Haiman Z., Rees M. J., Weinberg D. H., 2004, *ApJ*, 601, 666
- Ewen H. I., Purcell E. M., 1951, *Nature*, 168, 356
- Efstathiou G., 1992, *MNRAS*, 256, 43P
- Fan X., Narayanan V. K., Strauss M. A., White R. L., Becker R. H., Pentericci L., Rix H.-W., 2002, *AJ*, 123, 1247, arXiv:astro-ph/0111184
- Fan X., Strauss M. A., Becker R. H., 2006, *AJ*, 132, 117, arXiv:astro-ph/0512082v2
- Field G. B., 1958, *Proc. IRE*, 46, 240
- Field G. B., 1959, *ApJ*, 129, 536
- Friedrich M. M., Mellema G., Alvarez M. A., Shapiro P. R., Iliev I. T., 2011, *MNRAS*, 413, 1353, arXiv:1006.2016v2
- Furlanetto, S. R., Oh, S. P., 2005, *MNRAS*, 363, 1031, arXiv:astro-ph/0505065
- Furlanetto S. R., Peng Oh S., Briggs F. H., 2006, *Phys. Rep.*, 433, 181, arXiv:astro-ph/0608032v2
- Furlanetto S. R., Zaldarriaga M., Hernquist L. [FZH04], 2004, *ApJ*, 613, 1, arXiv:astro-ph/0403697
- Furlanetto S. R., Zaldarriaga M., Hernquist L., 2004, *ApJ*, 613, 16, arXiv:astro-ph/0404112v1
- Haiman Z., Abel T., Rees M. J., 2000, *ApJ*, 534, 11
- Harker G. J. A. et al., 2009, *MNRAS*, 393, 1449, arXiv:0809.2428v2
- Haslam C. G. T., Salter C. J., Stoffel H., Wilson W. E., 1982, *A&AS*, 47
- Heckman T. M. et al., 2011, *ApJ*, 730, 5, arXiv:1101.4219
- Ichikawa K., Barkana R., Iliev I. T., Mellema G., Shapiro P. R., 2010, *MNRAS*, 406, 2521, arXiv:0907.2932
- Iliev I. T., Mellema G., Ahn K., Shapiro P. R., Mao Y., Pen U.-L., 2013, preprint, p. 20, arXiv:1310.7463
- Jeans J., 1928, *Astronomy and Cosmogony*. Cambridge University Press
- Jenkins A., Frenk C. S., White S. D. M., Colberg J. M., Cole S., Evrard A. E., Couchman H. M. P., Yoshida N., 2001, *MNRAS*, 321, 372, arXiv:astro-ph/0005260
- Kim H.-S., Wyithe J. S. B., Park J., Lacey C. G., 2013, *MNRAS*, 433, 2476, arXiv:1303.3051
- Lacey C., Cole S., 1993, *MNRAS*, 262, 627
- Lidz A., Zahn O., McQuinn M., Zaldarriaga M., Hernquist L., 2008, *ApJ*, 680, 962, arXiv:0711.4373v1
- Lidz A., Faucher-Giguere C.-A., Dall'Aglio A., McQuinn M., Fechner C., Zaldarriaga M., Hernquist L., Dutta S., 2010, *ApJ*, 718, 199, arXiv:0909.5210
- Liu A., Pritchard J. R., Tegmark M., Loeb A., 2013, *Phys. Rev. D*, 87, 043002, arXiv:1005.4057
- Loeb, A., Furlanetto, S. R., 2013, *The First Galaxies in the Universe*, Princeton University Press
- Madau P., Meiksin A., Rees M. J., 1997, *ApJ*, 475, 429, arXiv:astro-ph/9608010
- McQuinn M., Zahn O., Zaldarriaga M., Hernquist L., Furlanetto S. R., 2006, *ApJ*, 653, 815, arXiv:astro-ph/0512263
- Mellema G., Iliev I. T., Pen U.-L., Shapiro P. R., 2006, *MNRAS*, 372, 679
- Mellema G. et al., 2013, *Exp. Astron.*, 36, 235, arXiv:1210.0197
- Mesinger, A., Ewall-Wice, A. & Hewitt, J., 2013, preprint, arXiv:1311.4574
- Mesinger A., Furlanetto S. R., 2007, *ApJ*, 669, 663, arXiv:0704.0946v1
- Mesinger A., Furlanetto S. R., Cen R., 2011, *MNRAS*, 411, 955, arXiv:1003.3878v1
- Miralda-Escude J., 2003, *ApJ*, 597, 66, arXiv:astro-ph/0211071
- Miralda-Escude J., Haehnelt M., Rees M. J. [MHR00], 2000, *ApJ*, 530, 1-16, arXiv:astro-ph/9812306
- Morales M. F., Wyithe J. S. B., 2010, *ARA&A*, 48, 127, arXiv:0910.3010
- Mortlock D. J. et al., 2011, *Nature*, 474, 616, arXiv:1106.6088
- Ono Y. et al., 2012, *ApJ*, 744, 83, arXiv:1107.3159
- Ota K. et al., 2010, *ApJ*, 722, 803, arXiv:1008.4842
- Pan T., Barkana R., 2012, preprint, arXiv:1209.5751
- Pentericci L. et al., 2011, *ApJ*, 743, 132, arXiv:1107.1376
- Petrovic N., Oh S. P., 2011, *MNRAS*, 413, 2103, arXiv:1010.4109v2
- Planck Collaboration: Ade P. A. R. et al., 2013, preprint, arXiv:1303.5076
- Pober J. C. et al., 2013, preprint, arXiv:1310.7031
- Pritchard, J. R., Furlanetto, S. R., 2007. *MNRAS*, 376, 1680, arXiv:astro-ph/0607234
- Pritchard J. R., Loeb A., 2008, *Phys. Rev. D*, 78, arXiv:0802.2102
- Pritchard J. R., Loeb A., 2011, *Progress Phys.*, p. 64, arXiv:1109.6012
- Prodel A., Kusch P., 1952, *Phys. Rev.*, 88, 184
- Robertson B. E. et al., 2013, *ApJ*, 768, 71, arXiv:1301.1228
- Schenker M. A., Stark D. P., Ellis R. S., Robertson B. E., Dunlop J. S., McLure R. J., Kneib J.-P., Richard J., 2012, *ApJ*, 744, 179, arXiv:1107.1261v2
- Sheth R. K., Tormen G., 1999, *MNRAS*, 308, 119, arXiv:astro-ph/9901122
- Storrie-Lombardi L. J., McMahon R. G., Irwin M. J., Hazard C., 1994, *ApJ*, 427, L13
- Theuns T., Schaye J., Zaroubi S., Kim T.-S., Tzanavaris P., Carswell B., 2002, *ApJ*, 567, L103, arXiv:astro-ph/0201514
- Tingay S. J. et al., 2013, *Publ. Astron. Soc. Australia*, 30, 1, arXiv:1206.6945
- Trott C. M., Wayth R. B., Tingay S. J., 2012, *ApJ*, 757, 101, arXiv:arXiv:1208.0646v1
- Wang X., Tegmark M., Santos M. G., Knox L., 2006, *ApJ*, 650, 529, arXiv:astro-ph/0501081
- Wyithe J. S. B., Morales M. F., 2007, *MNRAS*, 379, 1647, arXiv:astro-ph/0703070
- Zaldarriaga M., Furlanetto S. R., Hernquist L., 2004, *ApJ*, 608, 622, arXiv:astro-ph/0311514
- Zaroubi S. et al., 2012, *MNRAS*, 425, 2964
- Zel'dovich Y. B., 1970, *A&A*, 5, 84

APPENDIX A: ERROR ANALYSIS

When considering the errors on the moments of the brightness temperature PDF we take the values measured from the simulation to be the true statistic and then ask what happens when Gaussian random noise, independent but identically distributed, is introduced. The true moments in which we are interested in measuring are given by,

$\langle n_i \rangle$	$= 0$	
$\langle n_i n_j \rangle$	$\left. \begin{array}{l} \langle n_i^2 \rangle = \sigma_i^2 \quad (i = j) \\ \langle n_i \rangle \langle n_j \rangle = 0 \quad (i \neq j) \end{array} \right\}$	$\delta_{ij} \sigma_j^2$
$\langle n_i n_j^2 \rangle$	$\left. \begin{array}{l} \langle n_i^3 \rangle = 0 \quad (i = j) \\ \langle n_i \rangle \langle n_j^2 \rangle = 0 \quad (i \neq j) \end{array} \right\}$	0
$\langle n_i^2 n_j^2 \rangle$	$\left. \begin{array}{l} \langle n_i^4 \rangle = 3\sigma_i^4 \quad (i = j) \\ \langle n_i^2 \rangle \langle n_j^2 \rangle = \sigma_i^2 \sigma_j^2 \quad (i \neq j) \end{array} \right\}$	$(1 + 2\delta_{ij}) \sigma_i^2 \sigma_j^2$
$\langle n_i^2 n_j^3 \rangle$	$\left. \begin{array}{l} \langle n_i^5 \rangle = 0 \quad (i = j) \\ \langle n_i^2 \rangle \langle n_j^3 \rangle = 0 \quad (i \neq j) \end{array} \right\}$	0
$\langle n_i n_j^3 \rangle$	$\left. \begin{array}{l} \langle n_i^4 \rangle = 3\sigma_i^4 \quad (i = j) \\ \langle n_i \rangle \langle n_j^3 \rangle = 0 \quad (i \neq j) \end{array} \right\}$	$3\delta_{ij} \sigma_i^4$
$\langle n_i^3 n_j^3 \rangle$	$\left. \begin{array}{l} \langle n_i^6 \rangle = 15\sigma_i^6 \quad (i = j) \\ \langle n_i^3 \rangle \langle n_j^3 \rangle = 0 \quad (i \neq j) \end{array} \right\}$	$15\delta_{ij} \sigma_i^6$

Table A1. Some useful identities of the Gaussian noise assumed in our modelling of instrumental noise.

$$\begin{aligned}
 S_2 &= \frac{1}{N_{\text{pix}}} \sum_{i=0}^{N_{\text{pix}}} (\delta T_i - \overline{\delta T})^2, \\
 S_3 &= \frac{1}{N_{\text{pix}}} \sum_{i=0}^{N_{\text{pix}}} (\delta T_i - \overline{\delta T})^3, \\
 K_4 &= \frac{1}{N_{\text{pix}}} \sum_{i=0}^{N_{\text{pix}}} (\delta T_i - \overline{\delta T})^4,
 \end{aligned} \tag{A1}$$

describing the variance, skew and kurtosis respectively. The brightness temperature in the output boxes is the ‘true’ signal dT and its mean is $\overline{\delta T} = N_{\text{pix}}^{-1} \sum_{i=0}^{N_{\text{pix}}} \delta T_i$. We assume that what is actually measured, x , is the linear combination of true signal and noise n , i.e. in each pixel we have $x_i = \delta T_i + n_i$. In this construction we imagine our simulated maps represent some true observable signal in a region of the universe, which is then corrupted by random instrumental noise. In doing so we only consider the effects of noise and are neglecting the bias induced by sampling a restricted region of the universe.

We first considered whether there would be noise induced bias by testing a naive estimator of the m^{th} moment given by $N_{\text{pix}}^{-1} \sum_i^{N_{\text{pix}}} (x_i - \overline{x_i})^m$ where $\overline{x_i} = N_{\text{pix}}^{-1} \sum_i^{N_{\text{pix}}} x_i$. We assume throughout the standard properties of Gaussian random noise with a standard deviation of σ and a mean of 0. The even nature of Gaussian PDF returns 0 value even moments; odd moments are given by

$$\langle n^m \rangle = (1)(3)(5)\dots(m-1)\sigma^m, \tag{A2}$$

where the angle brackets denote an estimator over noise realisations of their contents. This is the interpretation throughout as we are assuming the signal to be ‘true’ and unchanging. Some useful identities are summarised in Table A1, all exploit the assumption that noise on different pixels is independent. We first consider the question of bias in the estimator, finding a bias is induced by our naive estimator for the variance of the noisy data but not for the

skewness.

$$\begin{aligned}
 \hat{S}_2^{\text{test}} &= \frac{1}{N_{\text{pix}}} \sum_{i=0}^{N_{\text{pix}}} (x_i - \overline{x})^2 \\
 &= \frac{1}{N_{\text{pix}}} \sum_{i=0}^{N_{\text{pix}}} [(\delta T_i - \overline{\delta T}) + n_i]^2; \\
 \langle \hat{S}_2^{\text{test}} \rangle &= \frac{1}{N_{\text{pix}}} \sum_{i=0}^{N_{\text{pix}}} (\delta T_i - \overline{\delta T})^2 + 2(\delta T_i - \overline{\delta T}) \langle n_i \rangle + \langle n_i^2 \rangle \\
 &= \frac{1}{N_{\text{pix}}} \sum_{i=0}^{N_{\text{pix}}} (\delta T_i - \overline{\delta T})^2 + \sigma_i^2.
 \end{aligned} \tag{A3}$$

If we assume that $\sigma_i^2 = \sigma_{\text{noise}}^2$ for all i then we can construct the following unbiased estimators,

$$\begin{aligned}
 \hat{S}_2 &= \frac{1}{N_{\text{pix}}} \sum_{i=0}^{N_{\text{pix}}} (x_i - \overline{x})^2 - \sigma_{\text{noise}}^2, \\
 \hat{S}_3 &= \frac{1}{N_{\text{pix}}} \sum_{i=0}^{N_{\text{pix}}} (x_i - \overline{x})^3.
 \end{aligned} \tag{A4}$$

We then get an expression for the variance of our estimators for the m^{th} moment by applying $V_{\hat{S}_m} = \langle \hat{S}_m \hat{S}_m^T \rangle - \langle \hat{S}_m \rangle^2$. As we previously established unbiased estimators the second term on the RHS of this equation is the statistic of interest squared. We choose to describe our estimators as \hat{S}_2 and \hat{S}_3 for the variance and the skewness of our brightness-temperature PDFs. We also define $\mu_i = \delta T_i - \overline{\delta T}$ for clarity, where $\overline{\delta T} = N_{\text{pix}}^{-1} \sum_{i=0}^{N_{\text{pix}}} \delta T_i$. The subject of our calculations $x_i - \overline{x}$ becomes $\mu_i + n_i$ so that $(x_i - \overline{x})^2 = (\delta T_i + n_i - \overline{\delta T})^2 = \mu_i^2 + 2\mu_i n_i + n_i^2$. We derive the variance of our \hat{S}_2 estimator as follows,

$$\begin{aligned}
 V_{\hat{S}_2} &= \left\langle \frac{1}{N_{\text{pix}}^2} \sum_{i=0}^{N_{\text{pix}}} \sum_{j=0}^{N_{\text{pix}}} [(\mu_i + n_i)^2 - \sigma_{\text{noise}}^2] \right. \\
 &\quad \left. [(\mu_j + n_j)^2 - \sigma_{\text{noise}}^2] \right\rangle - (S_2)^2.
 \end{aligned} \tag{A5}$$

We can further multiply this expression out and move the noise averaging brackets inside the summation,

$$\begin{aligned}
 V_{\hat{S}_2} &= \frac{1}{N_{\text{pix}}^2} \sum_{i=0}^{N_{\text{pix}}} \sum_{j=0}^{N_{\text{pix}}} \left[\mu_i^2 \mu_j^2 + 2\mu_i^2 \mu_j \langle n_j \rangle + \mu_i^2 \langle n_j^2 \rangle \right. \\
 &\quad + 2\mu_i \langle n_i \rangle \mu_j^2 + 4\mu_i \mu_j \langle n_i n_j \rangle + 2\mu_i \langle n_i n_j^2 \rangle \\
 &\quad + \langle n_i^2 \rangle \mu_j^2 + 2\langle n_i^2 n_j \rangle \mu_j + \langle n_i^2 n_j^2 \rangle \\
 &\quad - \sigma_{\text{noise}}^2 (\mu_i^2 + 2\mu_i \langle n_i \rangle + \langle n_i^2 \rangle) + \mu_j^2 + 2\mu_j \langle n_j \rangle + \langle n_j^2 \rangle \\
 &\quad \left. + \sigma_{\text{noise}}^4 \right] - (S_2)^2.
 \end{aligned} \tag{A6}$$

Making use of the identities in Table A1 this reduces to

$$\begin{aligned}
V_{\hat{S}_2} = & \frac{1}{N_{\text{pix}}^2} \sum_{i=0}^{N_{\text{pix}}} \sum_{j=0}^{N_{\text{pix}}} \left[\mu_i^2 \mu_j^2 + \mu_i^2 \sigma_j^2 + 4\mu_i \mu_j \delta_{ij} \sigma_j^2 \right. \\
& + \sigma_i^2 \mu_j^2 + 3\delta_{ij} \sigma_i^4 + (1 - \delta_{ij}) \sigma_i^2 \sigma_j^2 \\
& \left. - \sigma_{\text{noise}}^2 (\mu_i^2 + \sigma_i^2 + \mu_j^2 + \sigma_j^2) \right] \\
& + \sigma_{\text{noise}}^4 - (S_2)^2.
\end{aligned} \tag{A7}$$

We can reduce this further by making some summation operations, where delta functions effectively convert all indices from i to j or vice versa and we get,

$$\begin{aligned}
V_{\hat{S}_2} = & \left(S_2^2 + S_2 \frac{1}{N_{\text{pix}}} \sum_{j=0}^{N_{\text{pix}}} \sigma_j^2 + \frac{4}{N_{\text{pix}}^2} \sum_{i=0}^{N_{\text{pix}}} \mu_i^2 \sigma_i^2 \right. \\
& + \frac{1}{N_{\text{pix}}} \sum_{i=0}^{N_{\text{pix}}} \sigma_i^2 S_2 + \frac{3}{N_{\text{pix}}^2} \sum_{i=0}^{N_{\text{pix}}} \sigma_i^4 \\
& + \frac{1}{N_{\text{pix}}^2} \sum_{i=0}^{N_{\text{pix}}} \sum_{j=0}^{N_{\text{pix}}} \sigma_i^2 \sigma_j^2 - \frac{1}{N_{\text{pix}}^2} \sum_{i=0}^{N_{\text{pix}}} \sigma_i^4 \\
& \left. - S_2 \sigma_{\text{noise}}^2 - \frac{\sigma_{\text{noise}}^2}{N_{\text{pix}}} \sum_{i=0}^{N_{\text{pix}}} \sigma_i^2 - S_2 \sigma_{\text{noise}}^2 - \frac{\sigma_{\text{noise}}^2}{N_{\text{pix}}} \sum_{j=0}^{N_{\text{pix}}} \sigma_j^2 \right) \\
& + \sigma_{\text{noise}}^4 - (S_2)^2.
\end{aligned} \tag{A8}$$

Again assuming that $\sigma_i^2 = \sigma_{\text{noise}}^2$ for all i , a multitude of cancellation leave

$$V_{\hat{S}_2} = \frac{2}{N_{\text{pix}}} (2S_2 \sigma_{\text{noise}}^2 + \sigma_{\text{noise}}^4). \tag{A9}$$

An identical procedure can be used to obtain an expression for the variance on \hat{S}_3 :

$$V_{\hat{S}_3} = \frac{3}{N_{\text{pix}}} (3\sigma_{\text{noise}}^2 K_4 + 12S_2 \sigma_{\text{noise}}^4 + 5\sigma_{\text{noise}}^6). \tag{A10}$$

Because we consider the normalised skew in this paper it is necessary to consider how the errors we have so far calculated propagate on to the normalised quantity. For the error of a function $f(X, Y)$ of two non-independent variables X and Y , Taylor expansion about the expectation values for X and Y provides an approximation to the variance on $f(X, Y)$ as a function of the errors on X and Y ,

$$\begin{aligned}
V[f(X, Y)] \approx & \left(\frac{\partial f}{\partial X} \right)^2 V[X] + \left(\frac{\partial f}{\partial Y} \right)^2 V[Y] \\
& + 2 \left(\frac{\partial f}{\partial X} \right) \left(\frac{\partial f}{\partial Y} C[X, Y] \right),
\end{aligned} \tag{A11}$$

where we use V_X to denote the variance of a quantity, here X , and $C[X, Y] = \langle XY \rangle - \langle X \rangle \langle Y \rangle$ to describe the covariance of two quantities, e.g. X and Y . Partial derivatives are carried out fixing $X = \langle X \rangle$ or $Y = \langle Y \rangle$ as appropriate. The covariance between our skew \hat{S}_3 and variance \hat{S}_2 estimators can be calculated in much the same way as for the variance of each, resulting in

$$C_{\hat{S}_2 \hat{S}_3} = \frac{6}{N_{\text{pix}}} S_3 \sigma_{\text{noise}}^2. \tag{A12}$$

The variance of our estimator for the normalised skew, $\gamma_3 =$

\hat{S}_3 / \hat{S}_2 is found to be

$$V_{\gamma_3} \approx \frac{1}{(S_2)^2} V_{\hat{S}_3} + \frac{(S_3)^2}{(S_2)^4} V_{\hat{S}_2} - 2 \frac{S_3}{(S_2)^3} C_{\hat{S}_2 \hat{S}_3}, \tag{A13}$$

and for $\gamma'_3 = \hat{S}_3 / (\hat{S}_2)^{3/2}$ we have

$$V_{\gamma'_3} \approx \frac{1}{(S_2)^3} V_{\hat{S}_3} + \frac{9}{4} \frac{(S_3)^2}{(S_2)^5} V_{\hat{S}_2} - 3 \frac{S_3}{S_2^4} C_{\hat{S}_2 \hat{S}_3}. \tag{A14}$$

This paper has been typeset from a $\text{\TeX}/\text{\LaTeX}$ file prepared by the author.